THREE-DIMENSIONAL BEAM TRACKING FOR WIRLESS COMMUNICATION SYSTEMS

AN MPHIL THESIS

BY

ZICHEN QI

February 2019

UNIVERSITY OF SHEFFIELD

Three-Dimensional Beam Tracking for Wireless Communication Systems

by

Zichen Qi

B.Sc, MSc

A master thesis submitted in partial fulfilment
of the requirements for the award of
Master of Philosophy

February 2019

Supervisors:
Dr. Wei Liu
and
Dr. Jonathan M Rigelsford

Acknowledgement

> You can't cross the sea merely by standing and staring at the water. - Rabindranath Tagore

At this moment, I would like to thank my supervisor Dr Wei Liu for his precise advice, for his unconditional support through the whole process and his belief in me.

Furthermore, I am very grateful to my family. It is their love that helps me on this journey. Thank you.

Abstract

The narrow millimetre wave beam in future 5G networks is easily interrupted by the movement of mobile handsets. In this thesis, a novel three-dimensional (3-D) beam tracking method is proposed to achieve beam alignment between the access node (AN) and the user node (UN). The algorithm is achieved through rotation tracking and location tracking of the UN relative to AN's beam angle and location. Rotation tracking algorithm is operating within the location tracking algorithm to track the UN's rotation and the rotation data is used to update the location information as the UN moves. For rotation tracking, a gradient descent algorithm is employed for self-rotation tracking based on measurements obtained by the three smart phone sensors (gyroscope, accelerometer and magnetometer) embedded in the micro-electro-mechanical system (MEMS). For location tracking, an extended Kalman filtering (EKF) based location tracking algorithm is also incorporated into the design by combining the data from direction of arrival (DoA) and time of arrival (ToA) estimation results of the user node (UN), since accurate UN location information is also crucial in the beam tracking process. Moreover, an operation protocol is provided for the tracking process and tested in three different scenarios: self-rotation with a fixed UN position and one AN, self-rotation with the straight-line movement of the UN with one AN and self-rotation with the straight-line movement of six ANs.

Contents

List of Publications

1. Z. Qi and W. Liu. "Three-Dimensional Millimetre-wave Beam Tracking Based on Smart Phone Sensor Measurements and Direction of Arrival/Time of Arrival Estimation for 5G Networks." *IET Microwaves Antennas & Propagation*, vol. 12, no. 3, pp. 271-279, 2017.
2. Z. Qi and W. Liu. "Three-Dimensional Millimetre Wave Beam Tracking Based on Handset MEMS Sensors with Extended Kalman Filtering." *Proceedings of Radio Propagation & Technologies for 5G, IET*, Oct. 3, 2016, Durham, UK, pp. 1-6.

List of Acronyms

AN	Access Node
UN	User Node
MEMS	Micro-Elecro-Mechanical-Systems
DoA	Direction of Arrival
OTDoA	Obervered Difference of Arrival
ToA	Time of Arrival
TDoA	Time Difference of Arrival
RSS	Received Signal strength
MIMO	Multiple-Input Multiple-Output
GNSS	Global Navigation Satellite Systems
RMSE	Root Mean Square Error
EKF	Extended Kalman Filter
UKF	Unsent Kalman Filter
WCE	Wireless Capsule Endoscopy
SNR	Signal Noise Ratio
AoD	Angle of Arrival
IMU	Inertial Measurement Unit
URA	Uniform Rectangular Array
LoS, NLoS	Line of Sight, Non Line of Sight
DCM	Direction Cosine Matrix
NED	North East Down

List of Figures

Chapter 1

Introduction

In 5G ultra-dense networks, it is envisaged that the distance between the various access nodes (ANs) and user nodes (UNs) would be in the range of tens of meters or even less. As a result, UNs are mainly in the line of sight(LoS) communication with ANs [5]. However, due to the inherent property of millimetre wave for transmission and reception, the wavelength of the millimetre wave is extremely short, the beam alignment between the AN and the UN can be easily destroyed by even a slight movement of the UN, causing a significant loss of the received signal power. Therefore, the user's behavioural changes (self-rotation) and location information are essential for maintaining an acceptable level of the communication link between the AN and the UN. There exist several research projects that track the beam, but they depend on the channel information and some other network level feature. In this thesis, we will explain and propose a three-dimensional tracking algorithm based on the handset offering data. All fundamental theories to full implementation will be discussed in detail.

1.1 Ultra-Dense Networks

Ultra-Dense Networks(UDN) is defined as the quantity of ultra-small cells outnumbered that of active UNs [6]. The quantity measurement of ultra-dense networks cells is considered to be more than $10^3 cells/km^2$ [7]. Moreover, these ultra-small cells in UDN are expected to operate as a macro cell, but in a small coverage and much lower power supply. The ultra-small cell also has full functionality to perform transmission and communication. Additionally, an ultra-small cell in 5G UDN is expected to apply radio frame which can include the range from 0.1ms to 0.5ms [8]. Such a frame can consist of uplink reference symbols which can be used in network-centric localisation and information updates.

The distance between each AN is expected to be small ranging from a few metres to 50 metres in the ultra-dense small cell [9] . As a result, in such an UDN, it is possible to assume there are always at least one UN communicating with the AN in the line of sight. Besides, the 5G UDN will apply a distributed antenna systems, an architecture where several geographically dispersed antennas connected to an AN across one area, to further extend the communication coverage of each AN in low power and lower latency.

Moreover, the extremely short wavelength of millimetre wave renders installation of a large number of antenna arrays at both UNs and ANs possible. Those antennas are defined as the smart antenna which is mainly phased antenna array. Also, smart antenna enables massive multiple-input-multiple-output(MIMO) solution feasible in the future, which can be seen in [10] and [11], thus the transmission rate can be highly improved. The results showed in [12], with the number of antennas in a single array increases, the accuracy of DoA estimation has improved. Due to the massive amount of data in future 5G network, a high operation frequency is required. The current microwave frequencies can at best be doubled [11] in transmission rate, which would not be enough for 5G network communication. As mentioned earlier, high frequencies bring severe losses during transmission, but high frequencies also improve the accuracy of ToA estimation [13].

As the number of mobile phone users increased every year and the high-frequency millimetre wave is applied, both vertical and horizontal model of UDN are taken into considerations in [14] to deal with the poor penetration ability of millimeter wave. According to that, 3D-MIMO concept [15] has also given rise, and this new scheme can improve the 5G communication in the high-rise building with an ultra-dense crowd, which solve the problem by easily creating several lines of sight communication.

1.2 Positioning Methods

The lousy penetration property of millimetre wave requires accurate position information to dodge the possible obstacles in the transmission path. However, traditional commercial positioning techniques may not meet the requirements of 5G beam tracking, including the global navigation satellite systems(GNSSs) with a root mean square error(RMSE) of $5m$ [13], observed time difference of arrival(OTDoA) with an RMSE of about $25m$ [16], and WLAN fingerprinting of approximately $3m$ to $4m$ [17]. Also, the ultra-dense network of 5G makes a large number of antennas deployment possible, which enables ToA(time of arrival), RSS(received signal strength) and TDoA(time difference of arrival) [13] positioning method. However, individually applying DoA, RSS, ToA or TDoA to perform positioning task can only achieve an accuracy around 3 meters [13], which doesn't fulfil the system requirement. Also, some simple combinations of the above mentioned methods cannot fulfill the accuracy requirement perfectly [13].

Recently, combining the essential tracking methods with other tracking algorithms seems to have solved the problem. In the literature, Kalman filter and its variations are the popular choices nowadays. In [18], a joint DoA/ToA tracking method based on extended Kalman filtering (EKF) and a clock offset positioning method was proposed with an accuracy of about $0.1m$. The authors of [19] have proposed a novel UKF(unsent Kalman filter) with DoA and ToA and compared it with EKF(extended Kalman filter) regarding 3D positioning. Other than navigation on the road, [20] has explored the potential usage of combined ToA/DoA with Kalman filter in a single wireless capsule endoscopy(WCE) travelling along the gastrointestinal tract.

Furthermore, other tracking methods have also been tested. By combining DoA and RSS, a low-complexity localisation system was presented in [21]. The angle information acquired from DoA is applied in direction lock loop for tracking purposes in [22].

1.3 Rotation Tracking Methods

Rotation tracking plays an important role in various fields including human motion analysis [23, 24] , navigation [25, 26], robotics [27, 28] and aerospace [29–31] . Inertial-based Rotation measurement is a kind of self-contained method, of which any specific requirements of motion or environment setting are not needed. A typical IMU(Inertial Measurement Unit) consists of gyroscopes and accelerometers, which give rotational and attitude information. An IMU alone can give sufficient measurements in robots, navigation and aerial veicle [27,29,30]. A hybrid IMU would incorporate a compass or magnetometer to aid the rotation tracking.

Precisely, for a Hybrid IMU to measure a three-dimensional rotation, a tri-axis gyroscope, a tri-axis accelerometer and a tri-axis magnetometer are required. A gyroscope measures angular velocity, if the initial state is given, the rotation information can be calculated through integration over a short time in the scale of millimetre second [32,33]. An accurate gyroscope is too expensive and too large to be incorporated in a smart device, so a better way is to apply less precise gyroscope in a MEMS (Micro Electrical Mechanical System) [34].

No matter how accurate the gyroscope is, the integration of the gyroscope bias will cause the calculation error of rotation angle afterwards. Therefore, a single gyroscope is not able to give precise rotation measurement. As a result, an accelerometer and magnetometer have been introduced in the system as the reference signal trade-off for the gyroscope's measurement. The accelerometer will measure the acceleration, and the magnetometer will measure the magnetic field respectively. However, it is likely for these two sensors to be affected by high levels of disturbance(i.e: suddent acceleration and other magnetic fields). In this scenario, a sensor fusion algorithm needs to be applied. The Kalman filter is the favoured solution for the majority of the applications [35,36]. Although the widespread use of Kalman filter seems to be the best solution of the rotation track, it is very complicated to be implemented, which has been shown in [37–40]. The most complicated part of Kalman filter is the linear regression. Rotation tracking is a highly nonlinear process, which is difficult to be estimated. So that a linearised regression would be involved to simplify the calculation process.

Most of the smartphones nowadays are equipped with MEMs with all the essential sensors being incorporated. The minimum requirements for the installation are low, so MEMs become a popular choice for modern navigation products. The most recent development invention is virtual reality, such as Oculus rift [41]. It is the most advanced headset on the VR market, and it can trace the user's head's rotation direction by changing the image in the helmet accordingly. Kalman filter plays an important role in determining the orientation of Oculus rift [41].

1.4 Thesis Contribution

As an extension to [42], a three-dimensional(3-D) millimetre wave beam tracking method based on sensor fusion and extended Kalman filter was proposed in [43] and the results were only justified with the UN standing still at the same location. Also, the EKF applied in this paper requires complicated calculations, which would increase the workload of the smartphone and the network, as can be seen from the previous introduction.

In this thesis, a new 3-D tracking method is proposed to maintain the beam alignment between the AN and the UN in a 5G network using sensors embedded in smartphones. Compared to the work in [43], a gradient descent algorithm for rotation tracking based on [44] is applied in replace of EKF, which is a computationally efficient algorithm [44] and can achieve almost the same performance as or even better performance than the EKF with a lower computational complexity, and the proposed method is studied in more complicated scenarios, where a single user in an ultra-dense network with a LOS communication link moves. More specifically, a combination of DoA and ToA with extended Kalman filtering is used for location tracking; a uniform rectangular array(URA) is employed at the UN for 3-D beamforming, and its primary beam is adjusted towards the signal direction whenever it is below a preset threshold value; beam steering is employed for better performance instead of the fixed beam switching scheme adopted in [42].

For tracking behavioural changes (self-rotation) of the UN, we use the

Hybrid IMU of the smartphone to give self-measurements of the moving device. A Hybrid IMU includes a three-axis gyroscope (for measuring of angular velocity), a three-axis accelerometer, and a three-axis magnetometer, which are embedded in MEMS inside the smartphone. The data obtained from these sensors are incorporated by the gradient descent algorithm for tracking behavioural changes of the UN, where the gyroscope gives state update, while accelerometer and magnetometer provide measurement update to correct the gyroscope drift error. Besides, a protocol is proposed to provide specific instructions for the method to be implemented at the network and device level.

1.5 Thesis outline

Chapter 2 deals with the self-rotation tracking. The first two parts discuss the basic theories, quaternion representation, Euler angles and coordinate transform, used in the proposed algorithm which has been published in [45]. The last part gives ideas about three sensors which are gyroscope, accelerometer and magnetometer, and how these sensors operate. In the end of this chapter a rotation tracking algorithm has been given based on the work of [44] . Chapter 3 focuses on the positioning method. Basic tracking method ToA and DoA will be introduced in the first part. Then, localisation and tracking algorithm based on ToA and DoA will be discussed in detail with brief discussion of the antenna array used in the algorithm. The proposed sensor fusion tracking algorithm is presented with the test results and discussions in the end of this chapter. Chapter 4 gives the conclusion of this thesis. Chapter 5 discusses some of the potential research directions in this field.

Chapter 2

Self-Rotation Tracking

In this Chapter, we discuss the principles of the self-rotation tracking algorithm. To better understand the algorithm, some of the fundamental theories need to be addressed. The self-rotation tracking algorithm is mainly based on the application of quaternion, a mathematical tool used in particular for three-dimensional rotation calculations in a range of fields. The first section of this chapter will give the essential quaternion mathematical operation principles in association with the algorithm. The next section will present the Euler angles and the coordinate transform. The Euler angle is a crucial concept in describing rotation, mainly in aerospace orientation. Smartphone orientation also applies this theory with attitude in showing their positions to the users. So we use Euler angles to express the rotation with some transform through a quaternion, as the quaternion is hard to be viewed in a graph. The coordinate transforms is used to define the rotation tracking with a link to location tracking, as the two are in different frame systems [36]. The last section is about the self-rotation tracking algorithm. This algorithm is based on sensor fusion, which includes gyroscope, accelerometer and magnetometer. The basic operation and application principle of the sensors will be introduced to aid to better understand the algorithm.

2.1 Quaternion Representation

Quaternion algebra is widely used for defining the orientation of a rigid body or coordinated frame in a 3-D space. A quaternion is defined as a four-dimensional complex number [36].

An arbitrary orientation of frame k can be calculated through a rotation of angle α around a vector $\hat{\boldsymbol{r}}^n$ defined in frame n as showed in Fig.2.1. In Fig.2.1, mutually orthogonal unit vectors $\hat{\boldsymbol{x}}_n$, $\hat{\boldsymbol{y}}_n$, $\hat{\boldsymbol{z}}_n$, $\hat{\boldsymbol{x}}_k$, $\hat{\boldsymbol{y}}_k$, $\hat{\boldsymbol{z}}_k$ define the main axis for two frames n and k. The quaternion expressing the orientation ${}^n_k\hat{\boldsymbol{q}}$ can be defined by equation (2.1), where r_x, r_y and r_z describe the components of unit vector $\hat{\boldsymbol{r}}^n$ in frame n and α denotes the rotation angle.

The notation system applied in this thesis can be explained as follows: the front sub-script is the frame being expressed and the front super-script is the frame relative to.

The quaternion ${}^n_k\hat{\boldsymbol{q}}$ describes the orientation of frame k relative to frame n.

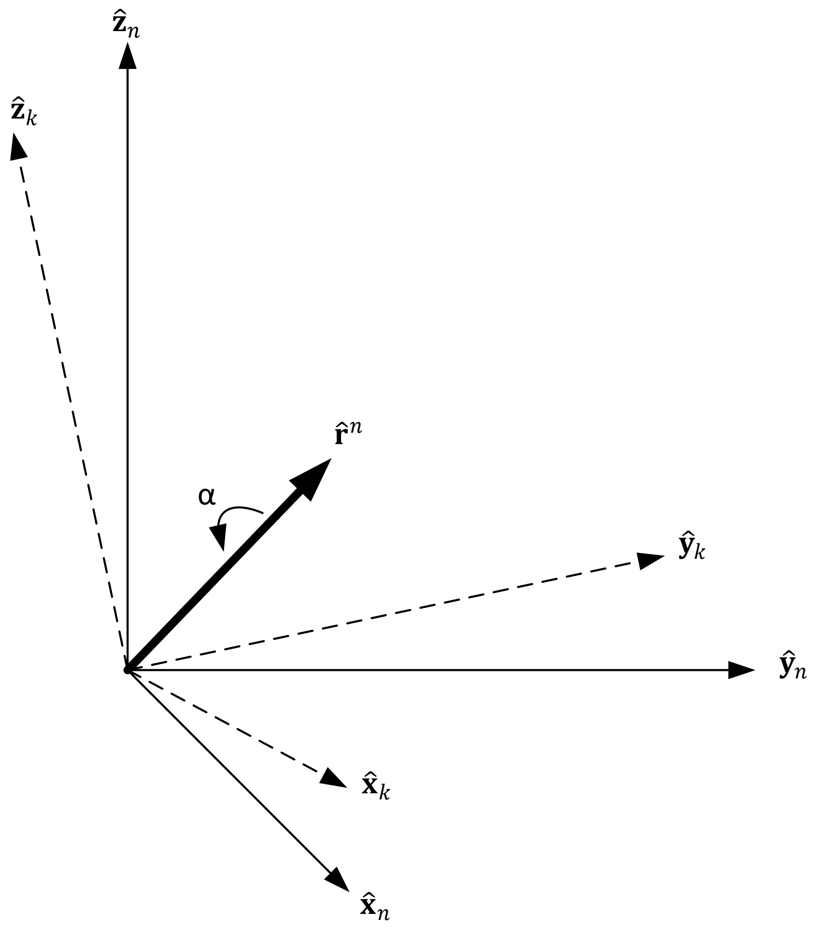

Fig. 2.1: The orientation of frame k is obtained by a rotation relative to frame n around the axis $\hat{\boldsymbol{r}}^n$.

$$ {}^n_k\hat{\boldsymbol{q}} = \begin{bmatrix} q_1 & q_2 & q_3 & q_4 \end{bmatrix} = \begin{bmatrix} \cos(\frac{\alpha}{2}) \\ -r_x * \sin(\frac{\alpha}{2}) \\ -r_y * \sin(\frac{\alpha}{2}) \\ -r_z * \sin(\frac{\alpha}{2}) \end{bmatrix}^T \tag{2.1} $$

The quaternion conjugate, denoted by *, can be applied to switch the two frames and is defined as

$$ {}^{n}_{k}\hat{\boldsymbol{q}}^{*} = {}^{k}_{n}\hat{\boldsymbol{q}} = \begin{bmatrix} q_1 \\ -q_2 \\ -q_3 \\ -q_4 \end{bmatrix}^{T} \tag{2.2} $$

Three dimensional vector $\mathbf{v}^n$ expressed in frame n can be switched to frame k through the following equation, and before the operation a 0 is put into $\mathbf{v}$ as the first element to make it as a four element vector.

$$ {}^{k}\boldsymbol{v} = {}^{n}_{k}\hat{\boldsymbol{q}} \otimes {}^{n}\boldsymbol{v}\, {}^{n}_{k}\hat{\boldsymbol{q}}^{*} \tag{2.3} $$

The quaternion product, denoted by $\otimes$, is an operation for multiple rotations. For example, rotation from frame n related to frame i can be achieved through the product of ${}^{k}_{i}\hat{\boldsymbol{q}}$ and ${}^{n}_{k}\hat{\boldsymbol{q}}$ in equation (2.4) to give the transformation quaternion ${}^{n}_{k}\hat{\boldsymbol{q}}$. Therefore, any vectors expressed in frame n can be changed to i by multiplying ${}^{n}_{i}\hat{\boldsymbol{q}}$.

$$ {}^{n}_{i}\hat{\boldsymbol{q}} = {}^{k}_{i}\hat{\boldsymbol{q}} \otimes {}^{n}_{k}\hat{\boldsymbol{q}} \tag{2.4} $$

The operation of quaternions $\boldsymbol{x}$ and $\boldsymbol{y}$'s product is under the Hamilton rule and is not commutative [46], i.e., $\boldsymbol{x} \otimes \boldsymbol{y} \neq \boldsymbol{y} \otimes \boldsymbol{x}$.

$$ \boldsymbol{x} \otimes \boldsymbol{y} = \begin{bmatrix} x_1 \\ x_2 \\ x_3 \\ x_4 \end{bmatrix}^{T} \otimes \begin{bmatrix} y_1 \\ y_2 \\ y_3 \\ y_4 \end{bmatrix}^{T} = \begin{bmatrix} x_1y_1 - x_2y_2 - x_3y_3 - x_4y_4 \\ x_1y_2 + x_2y_1 + x_3y_4 - x_4y_3 \\ x_1y_3 - x_2y_4 + x_3y_1 + x_4y_2 \\ x_1y_4 + x_2y_3 - x_3y_2 + x_4y_1 \end{bmatrix}^{T} \tag{2.5} $$

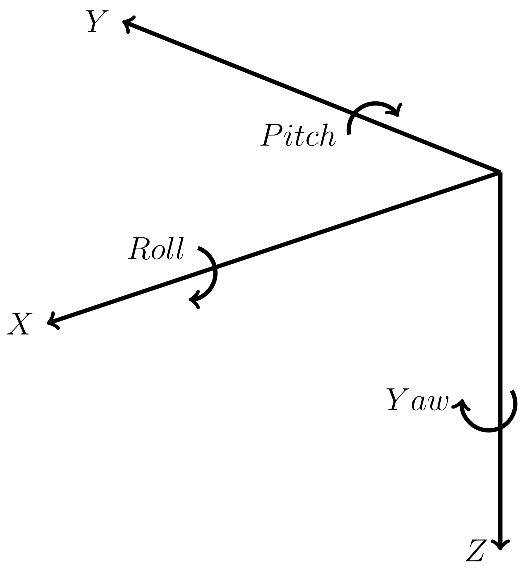

Fig. 2.2: Yaw, Pitch and Roll angles.

2.2 Euler Angles and Coordinate Transform

The popular rotation angle set of yaw-pitch-roll [4] (also expressed in z-y-x form) is chosen, as shown in Fig.2.2.

1. The rotation around z axis is defined by Yaw angle(marked as γ);
2. The rotation around y axis is defined by Roll angle(marked as β);
3. The rotation around x axis is defined by Pitch angle(marked as α);

All rotations can be expressed as a sequence with initial status $z_0 - y_0 - x_0$, first rotation $z_1 - y_1 - x_1$, second rotation $z_2 - y_2 - x_2$, and final rotation $z_3 - y_3 - x_3$, which can be seen in Fig.2.3.

The three rotation processes can be represented individually in the form of the Direction Cosine Matrix (DCM) or the rotation matrix as three basic clockwise rotations.

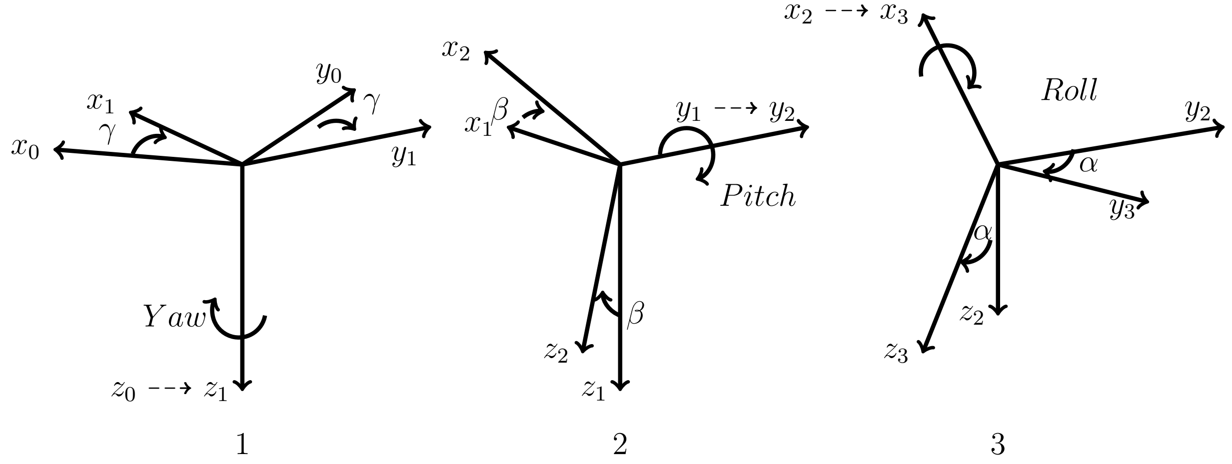

Fig. 2.3: Euler angles for z-y-x rotation sequence. Any predefined rotations can be reached by beginning at a reference orientation as in this example x_0, y_0, z_0, using specific rotation sequence Z-X-Y.

A yaw rotation around the z-axis is defined as

$$\mathbf{R}_z(\gamma) = \begin{bmatrix} \cos\gamma & -\sin\gamma & 0 \\ \sin\gamma & \cos\gamma & 0 \\ 0 & 0 & 1 \end{bmatrix} . \tag{2.6}$$

A pitch rotation around the y-axis is defined as

$$\mathbf{R}_y(\beta) = \begin{bmatrix} \cos\beta & 0 & \sin\beta \\ 0 & 1 & 0 \\ -\sin\beta & 0 & \cos\beta \end{bmatrix} . \tag{2.7}$$

A roll rotation around the x-axis is defined as

$$\mathbf{R}_x(\alpha) = \begin{bmatrix} 1 & 0 & 0 \\ 0 & \cos\alpha & -\sin\alpha \\ 0 & \sin\alpha & \cos\alpha \end{bmatrix} . \tag{2.8}$$

A combination of the three DCMs is often used to represent more complicated rotations :

$$\mathbf{R} = \begin{bmatrix} \cos\beta\cos\gamma & \cos\beta\sin\gamma & -\sin\beta \\ \sin\alpha\sin\beta\cos\gamma - \cos\alpha\sin\beta & sin\alpha\sin\beta\sin\gamma + \cos\alpha\cos\gamma & \sin\alpha\cos\beta \\ \cos\alpha\sin\beta\cos\gamma + \sin\alpha\sin\gamma & \cos\alpha\sin\beta\sin\gamma - \sin\alpha\cos\gamma & \cos\alpha\cos\beta \end{bmatrix} \tag{2.9}$$

Moreover the orientation described by a quaternion can be represented as the rotation matrix through the following equation

$$\mathbf{R} = \begin{bmatrix} 2q_1^2 - 1 + 2q_2^2 & 2(q_2q_3 + q_1q_4) & 2(q_2q_4 - q_1q_3) \\ 2(q_2q_3 - q_1q_4) & 2q_1^2 - 1 + 2q_3^2 & 2(q_3q_4 + q_1q_2) \\ 2(q_2q_4 + q_1q_3) & 2(q_2q_4 - q_1q_2) & 2q_1^2 - 1 + 2q_4^2 \end{bmatrix} \tag{2.10}$$

The Euler angles can be described by equations (2.11), (2.12) and (2.13) in the quaternion form.

$$\gamma = Atan2(2q_2q_3 - 2q_1q_4, 2q_1^2 + 2q_2^2 - 1) \tag{2.11}$$

$$\beta = -sin^{-1}(2q_2q_4 + 2q_1q_3) \tag{2.12}$$

$$\alpha = Atan2(2q_3q_4 - 2q_1q_2, 2q_1^2 + 2q_4^2 - 1) \tag{2.13}$$

and $atan2$ is a four-quadrant inverse tangent function [47]:

$$atan2(y,x) = \begin{cases} arcatan\frac{y}{x} & \text{if } x > 0, \\ \frac{\pi}{2} - arcatan\frac{x}{y} & \text{if } y > 0, \\ -\frac{\pi}{2} - arcatan\frac{x}{y} & \text{if } y > 0, \\ -arcatan\frac{y}{x} + / - \pi & \text{if } x < 0, \\ \text{undefined} & \text{if } x = y = 0, \end{cases} \tag{2.14}$$

K ANs are considered in an ultra-dense network for UN positioning. The location $P_{a,k} = (x_{a,k}, y_{a,k}, z_{a,k})$ of each AN defined in north-east-down (NED) local-level frame (LLF) is assumed to be known in advance with $k = 1, 2, \cdots, K$. The UN is defined in the rigid body frame of the smart phone. In the process of position tracking using EKF [48], the UN sends a pilot signal periodically to communicate with the ANs. Thereafter, measurements from ToA and DoA are gathered by the network to yield a UN position estimate.

The location information of the UN $P_{u,k} = (x_{u,k}, y_{u,k}, z_{u,k})$, $k = 1, 2, \cdots, K$, is also defined in NED. Thus, the line of sight vector, ${}^{l}\boldsymbol{l}$, is calculated as (2.15), where l represents line of sight.

$${}^{l}\boldsymbol{l} = P_{u,k} - P_{a,k} \tag{2.15}$$

so ${}^{l}\boldsymbol{l} = [x_{u,k} - x_{a,k} \quad y_{u,k} - y_{a,k} \quad z_{u,k} - z_{a,k}]^T$ and the LoS vector can be expressed with the Euler angle as follows, where b represents body frame.

$${}^{b}\boldsymbol{l} = {}^{l}_{b}\mathbf{R}\,{}^{l}\boldsymbol{l};. \tag{2.16}$$

2.3 Tracking from Sensors

In this section we discuss the basic principles of the sensors and the tracking algorithm of the sensor fusion. The theory of the sensors will be discussed briefly as it is not essential to understand this thesis.

The coordinate axis we have applied in this thesis is the same as that in the Android documentation [1], which is shown in Fig. 2.4.

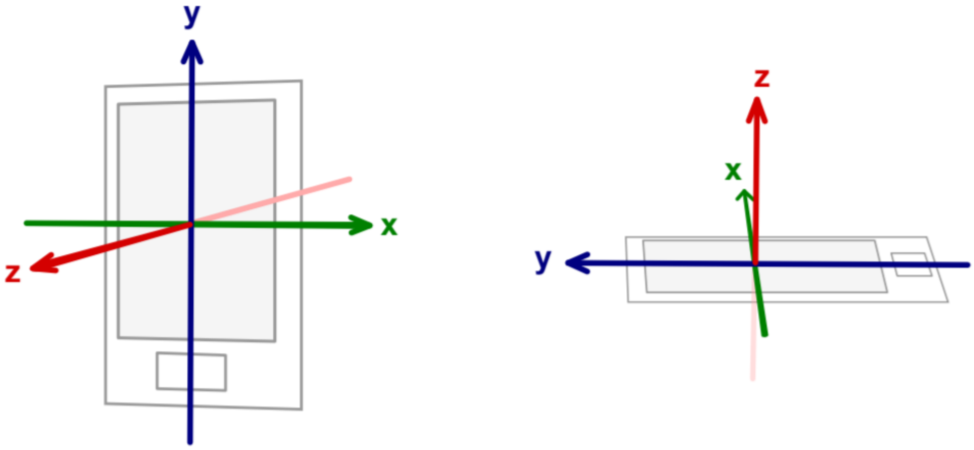

Fig. 2.4: Coordinate axis definition of android phones on Android Documentation [1].

2.3.1 Gyroscope

The traditional gyroscope is illustrated in Fig.2.5. This gyroscope is composed of a spinning disc inside several rings. Due to the angular momentum, the inside disc would keep rotating no matter what the orientation is of the gyroscope frame. Thus, the rotation angle could be determined by the difference between the disc and the ring.

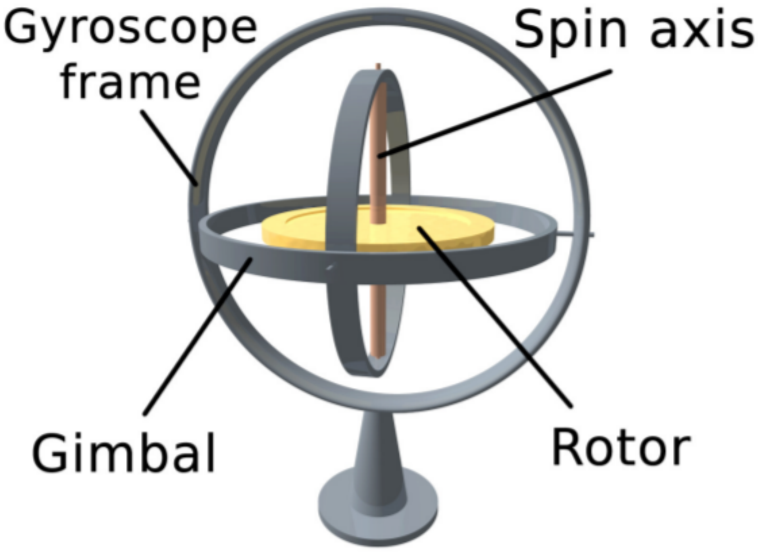

Fig. 2.5: Traditional gyroscope [2].

MEMS gyroscope consists of a set of vibrating elements to measure the Coriolis effect. The Coriolis effect is an inertial force that acts on objects in a rotation movement. It can be explained in Fig.2.6. When a reference frame is a rotation clockwise, and a mass is driven to vibrate along the driving axis, a force from the left will be put on the mass. Thus a secondary vibration will be incurred. The Coriolis effect describes the force, according to [49], the angular velocity can be calculated by the equation 2.17. It is essential to note that, the gyroscope measurement always references to the body, while the accelerometer measurement and magnetometer measurement are relative the earth.

$$F_c = -2m(\omega_g * v) \tag{2.17}$$

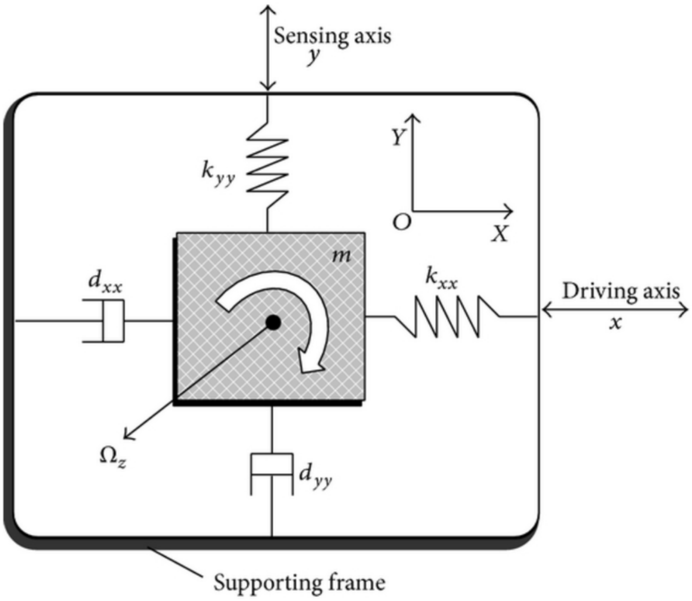

Fig. 2.6: The mechanism of gyroscope [2].

Most errors of gyroscopes are from the bias which is defined as the average output from the gyroscope when it is not moving. A constant bias error ϵ increases linearly with the time in integration. The typical solution to dealing with the error is to take a long-term average to estimate the constant bias. Thus, the estimated bias can be subtracted from the output.

2.3.2 Accelerometer

An accelerometer is a MEMS element that measures the acceleration of the object. In essence, the accelerometer measures the force on an object. Specifically, the accelerometer is like a mass attached with a spring at each direction (a 2D illustration is shown in Fig. 2.7). However, there is no actual mass in the MEMS; the theory remains the same. When an acceleration happens, there will be a displacement of the mass and the acceleration can estimate the acceleration due to the force from the spring. The accelerometer cannot distinguish the gravity and the upward acceleration. So to get the acceleration of an object due to a movement, the gravity needs to be subtracted. The most common error of the accelerometer is uncorrelated bias. The way to get rid of it is by moving average to smooth the output.

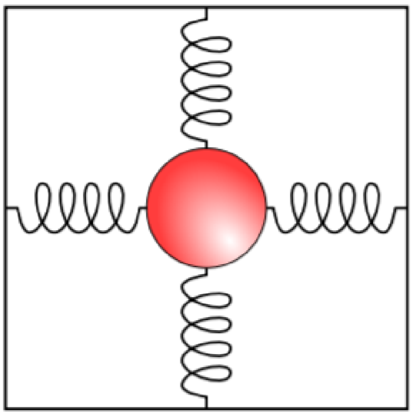

Fig. 2.7: Accelerometer concept in 2D [3].

2.3.3 Magnetometer

A magnetometer is a MEMS device to measure the magnetic field strength of the local area. There are two types of magnetometer: one is to measure the scalar, and the other is to measure the vector. The vector one is the standard using magnetometer.

Unlike the gyroscope and the accelerometer, the error of the magnetometer is mainly from outside. The magnetic disturbance is from the other components or other devices. The better way to decrease the error is to set a trade-off parameter and adjust it according to the text environment.

2.3.4 Rotation Tracking Algorithm

Although the gyroscope itself can measure the three rotation angles (yaw, pitch, roll) accurately in short time, the drift error caused by integration could cause significant errors in rotation tracking [50]. Besides, neither magnetometer nor accelerometer can give reliable measurements. As a result, measurements from the three sensors have to be combined by a gradient descent algorithm to achieve relatively high accuracy in rotation angle tracking. In detail, the quaternion estimation obtained from the gyroscope is corrected by a quaternion data obtained by the algorithm from the accelerometer and magnetometer.

The output of the gyroscope is angular rate. The measured angular rate of x, y and z axes is expressed as ω_x, ω_y and ω_z respectively. It can be expressed as follows in the quaternion form

$$\boldsymbol{\omega} = \begin{bmatrix} 0 & \omega_x & \omega_y & \omega_z \end{bmatrix} \tag{2.18}$$

In the algorithm, the Earth's field is known in the global frame, and the measurement of the relative relation between the global frame and the rigid body frame is needed to compute the rotation. The rotation data from the gyroscope at time t can be calculated by numerically integrating the quaternion derivative $\dot{\mathbf{q}}_{g,t}$ through equations (2.19) and (2.20) in the case of knowing the initial state.

$$ {}^B_G\dot{\boldsymbol{q}}_{g,t} = \frac{1}{2}\,{}^B_G\hat{\boldsymbol{q}}_{est,t-1} \otimes \boldsymbol{\omega}_t \tag{2.19} $$

$$ {}^B_G\dot{\boldsymbol{q}}_{g,t} = {}^B_G\hat{\boldsymbol{q}}_{est,t-1} + {}^B_G\dot{\boldsymbol{q}}_{g,t}\Delta t \tag{2.20} $$

In the above equations, ${}^B_G\boldsymbol{q}_{g,t}$ is the rotation of the smart phone measured at time t, Δt is the sampling period and ${}^B_G\hat{\boldsymbol{q}}_{est,t-1}$ is the previous estimate orientation, where ˆ indicates a normalized vector of unit length, and B and G represent the rigid body frame and the global frame, respectively.

The accelerometer will measure the earth's gravity, and similarly, the magnetometer will only measure the earth magnetic field at the beginning of the measurement. In the context of knowing the earth's magnetic field and gravity, all orientation related to the direction of the earth's frame will be calculated. Individually, the three-axis accelerometer measures the acceleration of each axis and transform the data into roll and pitch angles. The yaw angle (rotation around the z-axis) cannot be determined from the accelerometer [50] and the problem also exists in the calculation with the magnetometer, of which the rotation parallel with the earth's magnetic field cannot be determined. The way to solve this problem is to use optimisation formation.

By using a predefined reference direction ${}^G\hat{\boldsymbol{m}}$ in global frame, the frame transformation quaternion ${}^B_G\hat{\boldsymbol{q}}$ and the measured orientation ${}^B\hat{\boldsymbol{s}}$ in body frame, an optimization problem can by achieved with equation (2.3). Therefore the minimum ${}^B_G\hat{\boldsymbol{q}}$ which makes the solution of equation is the estimated optimum orientation. Equation (2.21) is the objective function and equation (2.22) to (2.24) describe parameters in the objective function.

$$\mathbf{f}({}^{B}_{G}\hat{\boldsymbol{q}}, {}^{G}\hat{\boldsymbol{m}}, {}^{B}\hat{\boldsymbol{s}}) = {}^{B}_{G}\hat{\boldsymbol{q}}^{\star} \otimes {}^{G}\hat{\boldsymbol{m}} \otimes {}^{B}_{G}\hat{\boldsymbol{q}} - {}^{B}\hat{\boldsymbol{s}} \tag{2.21}$$

$${}^{B}_{G}\hat{\boldsymbol{q}} = [q_1 \quad q_2 \quad q_3 \quad q_4] \tag{2.22}$$

$${}^{G}\hat{\boldsymbol{m}} = [0 \quad m_x \quad m_y \quad m_z] \tag{2.23}$$

$${}^{B}\hat{\boldsymbol{s}} = [0 \quad s_x \quad m_y \quad m_z] \tag{2.24}$$

Equation (2.25) is the gradient function of N iterations based on the initial guess ${}^{B}_{G}\hat{\boldsymbol{q}}_n$ to get the estimated orientation ${}^{B}_{G}\hat{\boldsymbol{q}}_{n+1}$ with a step size μ. Equation (2.26) calculates the gradient based on the objective function and the Jacobian matrix where equation (2.27) and (2.28) define the simplified objective function and the Jacobian matrix respectively. Equation (2.21) to (2.28) are the general solution form of the optimization problem with the accelerometer and magnetometer.

$${}^{B}_{G}\hat{\boldsymbol{q}}_{n+1} = {}^{B}_{G}\hat{\boldsymbol{q}}_{n} - \mu \frac{\nabla \boldsymbol{W}({}^{B}_{G}\hat{\boldsymbol{q}}, {}^{G}\hat{\boldsymbol{m}}, {}^{B}\hat{\boldsymbol{s}})}{\nabla \|\boldsymbol{W}({}^{B}_{G}\hat{\boldsymbol{q}}, {}^{G}\hat{\boldsymbol{m}}, {}^{B}\hat{\boldsymbol{s}})\|}, n = 0, 1, 2...N \tag{2.25}$$

$$\nabla \boldsymbol{W}({}^{B}_{G}\hat{\boldsymbol{q}}, {}^{G}\hat{\boldsymbol{m}}, {}^{B}\hat{\boldsymbol{s}}) = \mathbf{Z}^{T}({}^{B}_{G}\hat{\boldsymbol{q}}_{k}, {}^{G}\hat{\boldsymbol{m}}) \mathbf{W}({}^{B}_{G}\hat{\boldsymbol{q}}, {}^{G}\hat{\boldsymbol{m}}, {}^{B}\hat{\boldsymbol{s}}) \tag{2.26}$$

$$\mathbf{W}({}^{B}_{G}\hat{\boldsymbol{q}}, {}^{G}\hat{\boldsymbol{m}}, {}^{B}\hat{\boldsymbol{s}}) = \left[\begin{matrix} 2m_x(0.5 - q_3^2 - q_4^2) + \\ 2m_x(q_2q_3 - q_1q_4) + \\ 2m_x(q_1q_3 + q_2q_4) + \end{matrix}\right.$$

$$\left.\begin{matrix} 2m_z(q_2q_4 - q_1q_3) - s_x \\ 2m_z(q_1q_2 + q_3q_4) - s_y \\ 2m_z(0.5 - q_2^2 - q_3^2) - s_z \end{matrix}\right] \tag{2.27}$$

$$\mathbf{Z}({}^{B}_{G}\hat{\boldsymbol{q}}, {}^{G}\hat{\boldsymbol{m}}) = \left[\begin{matrix} 2m_yq_4 - 2m_zq_3 & 2m_yq_3 + 2m_zq_4 \\ -2m_xq_4 + 2m_zq_2 & 2m_xq_3 - 4m_yq_2 + 2m_zq_1 \\ 2m_xq_3 - 2m_yq_2 & 2m_xq_4 - 2m_yq_1 - 4m_zq_2 \end{matrix}\right.$$

$$\left.\begin{matrix} -4m_xq_3 + 2m_yq_2 - 2m_zq_1 & -4m_xq_4 + 2m_yq_1 + 2m_zq_2 \\ 2m_xq_2 + 2m_zq_4 & -2m_xq_1 - 4m_yq_4 + 2m_zq_3 \\ 2m_xq_1 + 2m_yq_4 - 4m_zq_3 & 2m_xq_2 + 2m_yq_3 \end{matrix}\right] \tag{2.28}$$

The output of the accelerometer is given by equation (2.29). The objective function and Jacobian equation can be defined through (2.30), (2.31) and (2.32), where ${}^{B}_{G}\hat{\boldsymbol{q}}$ is the frame transformation quaternion.

$$\boldsymbol{a\hat{c}c} = [0 \quad a_x \quad a_y \quad a_z] \tag{2.29}$$

$${}^{B}_{G}\hat{\boldsymbol{q}} = [q_1 \quad q_2 \quad q_3 \quad q_4] \tag{2.30}$$

$$\mathbf{W}_{acc}({}^{B}_{G}\hat{\boldsymbol{q}}, \boldsymbol{a\hat{c}c}) = \begin{bmatrix} 2(q_2q_4 - q_1q_3) - a_x \\ 2(q_1q_2 + q_3q_4) - a_y \\ 2(\frac{1}{2} - q_2^2 - q_3^2) - a_z \end{bmatrix} \tag{2.31}$$

$$\mathbf{Z}_{acc}({}^{B}_{G}\hat{\boldsymbol{q}}) = \begin{bmatrix} -2q_3 & 2q_4 & -2q_1 & 2q_2 \\ 2q_2 & 2q_1 & 2q_4 & 2q_3 \\ 0 & -4q_2 & -4q_3 & 0 \end{bmatrix} \tag{2.32}$$

The magnetometer measures the magnetic field. However, the magnetometer can be easily affected by other magnetic field [50]. The Earth magnetic field can be considered to have two components: the vertical component and the horizontal component, which are represented in equation (2.34). The output of the magnetometer measurement is given in (2.33). The objective function and Jacobian equation are defined in (2.35) and (2.36). The magnetic distortion is compensated by (2.37) and (2.38), where c_t is the compensated Earth magnetic field at time instant t.

$$\boldsymbol{m\hat{a}g} = [0 \quad b_x \quad b_y \quad b_z] \tag{2.33}$$

$$\boldsymbol{b}_e = [0 \quad b_{ex} \quad 0 \quad b_{ez}] \tag{2.34}$$

$$\mathbf{W}_{m\hat{a}g}({}^{B}_{G}\hat{\boldsymbol{q}}, \hat{\boldsymbol{b}}_e, \boldsymbol{m\hat{a}g}) = \begin{bmatrix} 2b_{ex}(0.5 - q_3^2 - q_4^2) + 2b_{ez}(q_2q_4 - q_1q_3) - b_x \\ 2b_{ex}(q_2q_3 - q_1q_4) + 2b_{ez}(q_1q_2 + q_3q_4) - b_y \\ 2b_{ex}(q_1q_3 + q_2q_4) + 2b_{ez}(0.5 - q_2^2 - q_3^2) - b_z \end{bmatrix} \tag{2.35}$$

$$\mathbf{Z}_{m\hat{a}g}({}^{B}_{G}\hat{\boldsymbol{q}}, \hat{\boldsymbol{b}}_e) = \begin{bmatrix} -2b_{ex}q_3 & 2b_{ez}q_4 & -4b_{ex}q_3 - 2b_{ez}q_1 & -4b_{ex}q_4 + 2b_{ez}q_2 \\ -2b_{ex}q_4 + 2b_{ez} & 2b_{ex}q_3 + 2b_{ez}q_1 & 2b_{ex}q_2 + 2b_{ez}q_4 & -2b_{ex}q_1 + 2b_{ez}q_3 \\ 2b_{ex} & 2b_{ex} - 4b_{ez}q_2 & 2b_{ex}q_1 - 4b_{ez}q_3 & 2b_{ex}q_2 \end{bmatrix} \tag{2.36}$$

$$\hat{\boldsymbol{n}}_t = [0 \quad n_x \quad n_y \quad n_z] = {}^{B}_{G}\hat{\boldsymbol{q}}_{est,t-1} \otimes \boldsymbol{m\hat{a}g} \otimes {}^{B}_{G}\hat{\boldsymbol{q}}^{\star}_{est,t-1} \tag{2.37}$$

$$\boldsymbol{c}_t = [0 \quad \sqrt{n_x^2 + n_y^2} \quad 0 \quad n_z] \tag{2.38}$$

The data from the accelerometer and magnetometer is combined by equations (2.39) and (2.40) and substituting $\boldsymbol{b}_e$ with $\boldsymbol{c}_t$.

$$\mathbf{W}_{acc,mag}({}^{B}_{G}\hat{\boldsymbol{q}}, \boldsymbol{a\hat{c}c}, \hat{\boldsymbol{c}}_t, \boldsymbol{m\hat{a}g}) = \begin{bmatrix} \mathbf{W}_{acc}({}^{B}_{G}\hat{\boldsymbol{q}}, \boldsymbol{a\hat{c}c}) \\ \mathbf{W}_{mag}({}^{B}_{G}\hat{\boldsymbol{q}}, \hat{\boldsymbol{c}}_t, \boldsymbol{m\hat{a}g}) \end{bmatrix} \tag{2.39}$$

$$\mathbf{Z}_{acc,mag}({}^{B}_{G}\hat{\boldsymbol{q}}, \hat{\boldsymbol{c}}_t) = \begin{bmatrix} \mathbf{Z}^{T}_{acc}({}^{B}_{G}\hat{\boldsymbol{q}}) \\ \mathbf{Z}^{T}_{mag}({}^{B}_{G}\hat{\boldsymbol{q}}, \hat{\boldsymbol{c}}_t) \end{bmatrix} \tag{2.40}$$

The process of the gradient descent algorithm is shown as follows, where ∇ represents the gradient operation and β is the magnitude of the error of the gyroscope measurement:

$${}^{B}_{G}\mathbf{q}_{est,t} = {}^{B}_{G}\hat{\boldsymbol{q}}_{est,t-1} + {}^{B}_{G}\dot{\boldsymbol{q}}_{est,t}\Delta t \tag{2.41}$$

$$ {}^{B}_{G}\dot{\boldsymbol{q}}_{est,t} = {}^{B}_{G}\dot{\boldsymbol{q}}_{g,t} - \beta\frac{\nabla W}{\nabla\|W\|} \tag{2.42} $$

$$ \nabla W = \begin{cases} \mathbf{Z}^{T}_{acc}({}^{B}_{G}\hat{\mathbf{q}}_{est,t-1})\mathbf{W}_{acc}({}^{B}_{G}\hat{\boldsymbol{q}}_{est,t-1}, \boldsymbol{a\hat{c}c}_{t}) \\ \mathbf{Z}^{T}_{acc,mag}({}^{B}_{G}\hat{\boldsymbol{q}}_{est,t-1}, \hat{\boldsymbol{c}}_{t}) \\ \Rightarrow \mathbf{W}_{acc,mag}({}^{B}_{G}\hat{\boldsymbol{q}}_{est,t-1}, \boldsymbol{a\hat{c}c}_{t}, \hat{\boldsymbol{c}}_{t}, \boldsymbol{m\hat{a}g}_{t}) \end{cases} \tag{2.43} $$

In this thesis, an additional drift bias compensation method is added to the algorithm to get rid of the gyroscope bias. The method is proceeded by defining the error ${}^{B}\boldsymbol{\omega}_{e,t}$ as the angular rate error though the inverse version of equation (2.19). The gyroscope bias ${}^{B}\boldsymbol{\omega}_{b,t}$ is defined by the integral of the angular error rate. As a result, the angular rate used in gradient descent algorithm is defined as ${}^{B}\boldsymbol{\omega}_{c,t}$ by subtracting bias from the raw data ${}^{B}\boldsymbol{\omega}_{t}$. Fig.2.8 shows a flowchart [45] of the gradient descent algorithm with gyroscope bias compensation.

$$ {}^{B}\boldsymbol{\omega}_{e,t} = 2\,{}^{B}_{G}\hat{\boldsymbol{q}}^{\star} \otimes \frac{\nabla W}{\nabla\|W\|} \tag{2.44} $$

$$ {}^{B}\boldsymbol{\omega}_{b,t} = \lambda\sum_{t}{}^{B}\boldsymbol{\omega}_{e,t}\Delta t \tag{2.45} $$

$$ {}^{B}\boldsymbol{\omega}_{c,t} = {}^{B}\boldsymbol{\omega}_{t} - {}^{B}\boldsymbol{\omega}_{b,t} \tag{2.46} $$

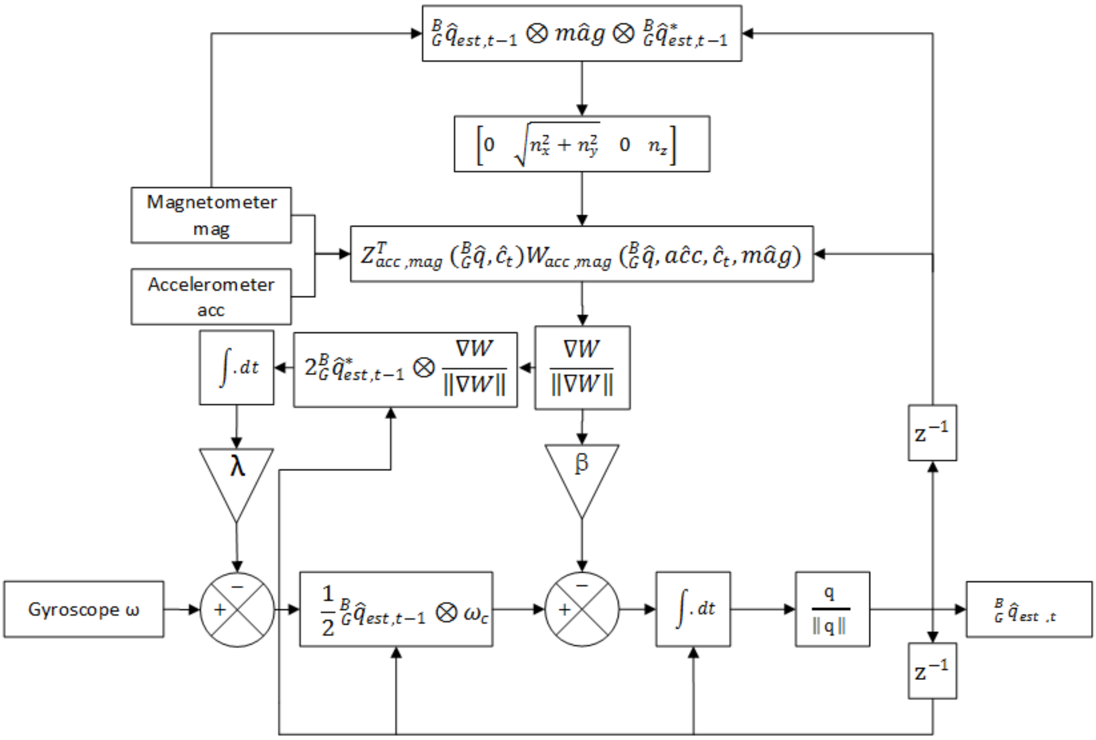

Fig. 2.8: Flowchart of the gradient descent algorithm. Gyroscope calculates the rough estimation of rotations while Magnetometer and Accelerometer correct through ${}^B_G\mathbf{q}_{est,t}$ update.

Chapter 3

Localisation and Tracking of the UN

The goal of this chapter is to describe the UN location tracking theory. ToA and DoA are described in the first section. ToA is a positioning technique, and it individually can give an estimation of the UN's location [45]. DoA is the method to estimate the arriving signal angle based on the signal strength. These two methods will be discussed thoroughly in this thesis. We have applied extended Kalman filter to fuse these two methods, as these two can only give rough estimations. Extended Kalman filter is a nonlinear version of Kalman filter. Although the complication of applying in rotation tracking has been discussed in several papers, the location tracking problem is way simple than the rotation tracking. Because of the simplicity, we have omitted the influence from the environment. The last part of this chapter will introduce the antenna array we have applied in our thesis. For the sake of simplicity, a rectangular array with hamming weight is applied. The application of this array is only for a simple three-dimensional tracking.

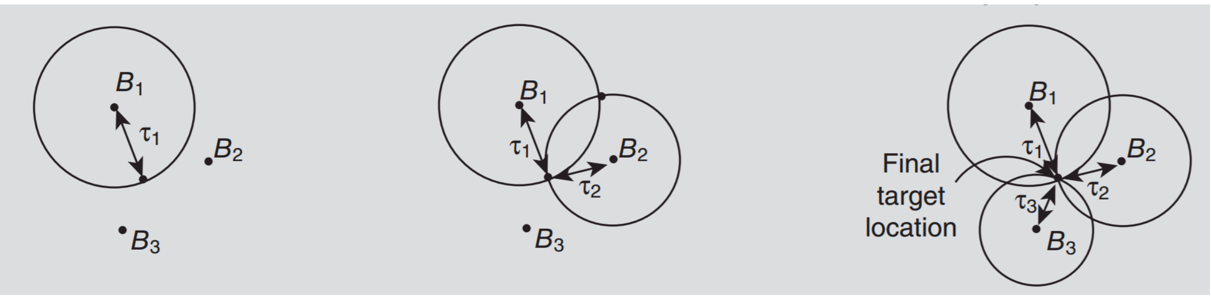

Fig. 3.1: Illustration of ToA localisation from [4].

3.1 ToA and DoA

The tracking methods we have applied in localisation are the time of arrival and direction of arrival. Before digging into the tracking algorithm, the fundamental theories of ToA and DoA need to be explained.

ToA can be defined as the travelling time between the AN and the UN in one way communication [45]. To get the most accurate results, the clock in the receiver and the sender need to be highly synchronised. However, if a round trip communication is applied, such synchronization can be replaced by a time difference trade-off [45]. The travelling time multiplying the speed of light gives the distance between the AN and the UN. The process of ToA horizontal localisation can be illustrated in the following figure 3.1. B1, B2 and B3 are ANs, $\tau 1, \tau 2$ and $\tau 3$ are travelling times. Each ToA corresponds to a circle where the AN is at the centre of it, and the UN is lying on the circle. Two ToA circles must have two intersections: one is the UN is the real location, and the other is not. As a result, at least three nodes are needed to cooperate to give a position of a UN. The vertical localisation process is the same as the horizontal one. However, in the scenario of disturbance, these circles may have multiple intersections. ToA positioning method may not be a perfect idea for tracking. However, with the help of DoA, using ANs to determine the angle of the arriving signal, this problem might be solved. The large scale of MIMO applied in 5G allows highly accurate DoA estimation, which gives the inclination and azimuth angles. The results can be multiplied with the distance measured in ToA, so only one AN is needed to give a location of the UN, given the location of AN known.

3.2 Localisation and Tracking Algorithm

Different from the tracking method employing several ANs in [48], we assume the UN communicates with only one base station at each time, since a single AN with TOA/DOA method in 5G ultra-dense network is sufficient for the tracking process.

The state vector of a UN is defined as $\boldsymbol{s}[i] = [x[i], y[i], z[i], \dot{x}[i], \dot{y}[i], \dot{z}[i]]^T$ which evolves from the dynamic model

$$\boldsymbol{s}[i] = f(\boldsymbol{s}[i-1]) \tag{3.1}$$

where $\boldsymbol{s}[i]$ consists of the UN's location and velocity state at time step i changing with the function $f(.)$ with covarience $\mathbf{Q}$

The measurement equation is composed of the DoA and ToA of the kth AN, which are modelled as $\hat{a}_k[i] = a_k[i] + e_{a,k}[i]$ and $\hat{t}_k[i] = t_k[i] + e_{t,k}[i]$, respectively, with estimation error $e_{a,k}$ and $e_{t,k}$, of which, $a_k[i]$ denotes the

2-D DoA angle θ and ϕ. Hence, the measurement vector y_k is written with the link to the state vector as

$$\boldsymbol{y}_k = [\hat{a}_k[i], \hat{t}_k[i]]^T = \boldsymbol{h}_k(s[i]) + \boldsymbol{m}[i] \tag{3.2}$$

where $h_k(.)$ is the handling function , and $\boldsymbol{m}[i] = [e_{a,k}[i], e_{t,k}[i]]^T$ with a noise covariance matrix $\mathbf{R}_k$. The relationship between the state vector and the measurement vector is

$$\hat{t}_k[i] = \frac{\sqrt{\Delta^2 x_k[i] + \Delta^2 y_k[i] + \Delta^2 z_k[i]}}{c}, \tag{3.3}$$

$$\hat{a}_k[i] = \begin{cases} \theta = \arctan \dfrac{\sqrt{\Delta^2 x_k[i] + \Delta^2 y_k[i]}}{\Delta z[i]} \\ \phi = \arctan \dfrac{\Delta y_k[i]}{\Delta x[i]} \end{cases} \tag{3.4}$$

where $\Delta x_k[i] = x[i] - x_{a,k}$, $\Delta y_k[i] = y[i] - y_{a,k}$, $\Delta z_k[i] = z[i] - z_{a,k}$ can then be represented in a compact form as,

$$\mathbf{Y}[i] = \boldsymbol{h}(s[i]) + \boldsymbol{m}[i] \tag{3.5}$$

where $\mathbf{Y} = [y_1^T, y_2^T, ..., y_K^T]$ and $\boldsymbol{h} = [h_1^T, h_2^T, ..., h_K^T]$ are the measurement equation at time-step i by combining the y_k into i*1 vector.

The estimation process is then expressed by the following equations:

$$\hat{\boldsymbol{s}}^-[i] = \begin{bmatrix} 1 & 0 & 0 & \Delta t & 0 & 0 \\ 0 & 1 & 0 & 0 & \Delta t & 0 \\ 0 & 0 & 1 & 0 & 0 & \Delta t \\ 0 & 0 & 0 & 1 & 0 & 0 \\ 0 & 0 & 0 & 0 & 1 & 0 \\ 0 & 0 & 0 & 0 & 0 & 1 \end{bmatrix} * \hat{\boldsymbol{s}}^+[i-1] + \boldsymbol{q}^+[i] \tag{3.6}$$

$$\mathbf{P}^{-}[i] = \mathbf{A}\mathbf{P}^{+}[i]\mathbf{A}^{T} + \mathbf{Q}[i] \tag{3.7}$$

For simplicity, the function of the target's movement has been modeled as a linear and discrete Wiener velocity model in equation (3.6) to denote the posteriori estimate and $\boldsymbol{q}$ and $\mathbf{P}$ are the process noise and the process covariance matrix representing the errors in estimate process, respectively.

The update process with new measurement is given by

$$\mathbf{K}[i] = \frac{\mathbf{P}^{-}[i]\mathbf{H}[i]}{\mathbf{H}[i]\mathbf{P}^{-}[i]\mathbf{H}^{T}[i] + \mathbf{R}[i]} \tag{3.8}$$

$$\hat{\boldsymbol{s}}^{+}[i] = \hat{\boldsymbol{s}}^{-}[i] + \mathbf{K}[i][\mathbf{Y}[i] - \mathbf{H}h(\hat{\boldsymbol{s}}^{-}[i])] \tag{3.9}$$

$$\mathbf{P}^{+}[i] = (\mathbf{I} - \mathbf{K}[i]\mathbf{H}[i])\mathbf{P}^{-}[i] \tag{3.10}$$

where $\mathbf{K}$ is the Kalman gain and $\mathbf{I}$ is the identity matrix. In equations (3.7) - (3.10), $\mathbf{H}$ and $\mathbf{A}$ are both obtained from Jacobian matrices.

$$\mathbf{A}[i] = \frac{\partial f[i]}{\partial s[i]} \tag{3.11}$$

$$\mathbf{H}[i] = \frac{\partial h[i]}{\partial s[i]} \tag{3.12}$$

Finally, the estimated position of UN is obtained as $\boldsymbol{s}^{+}[i] = (x^{+}[i], y^{+}[i], z^{+}[i])$ with the update process covariance matrix $\mathbf{P}^{+}$.

3.3 Rectangular Array

At the smart phone, a 11×11 uniform rectangular array (URA) [51] consisting of patch antennas is employed for beam steering. The response of a URA can be written as

$$B(\psi_x,\psi_y)=e^{-j(\frac{N-1}{2}\psi_x+\frac{M-1}{2}\psi_y)}\sum_{m=0}^{M-1}\sum_{n=0}^{N-1}w_{nm}^{*}e^{j(n\psi_x+m\psi_y)} \tag{3.13}$$

where

$$\psi_x=\frac{2\pi}{\lambda}\sin\theta\cos\phi \tag{3.14}$$

$$\psi_y=\frac{2\pi}{\lambda}\sin\theta\sin\phi \tag{3.15}$$

Each row has N elements while each column has M elements, with $d_x = d_y = \lambda/2$ and θ and ϕ representing azimuth and elevation angles, respectively. The beam pattern of a uniform weighting rectangular array has relatively high side lobe levels. Therefore, the Hamming weight is applied to suppress the side lobes .

The function for Hamming weighting is

$$\begin{aligned} w_x(n)=w_y(n)=g_0+g_1\cos\frac{2\pi n}{N},\\ n=-\frac{N-1}{2},...,\frac{N-1}{2} \end{aligned} \tag{3.16}$$

The coefficients g_0 and g_1 is determined for the array pattern to have a null at $\frac{1}{3}$. So the final function can be written as

$$\begin{aligned} w_x(n)=w_y(n)=0.54+0.46\cos\frac{2\pi n}{N},\\ n=-\frac{N-1}{2},...,\frac{N-1}{2} \end{aligned} \tag{3.17}$$

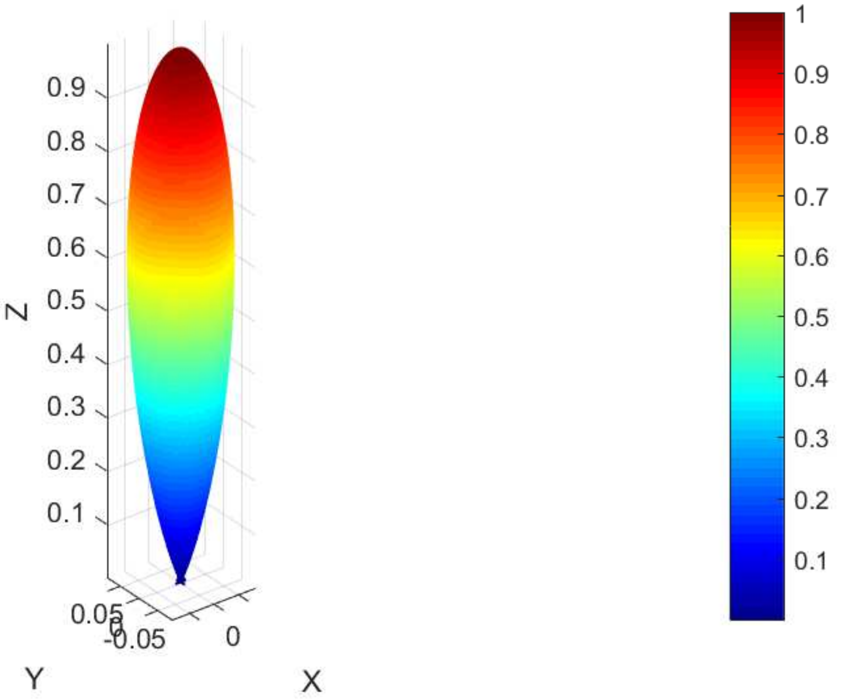

Fig. 3.2: Magnitude beam response of 11×11 rectangular array with Hamming weight. A narrow beam is presented to provide more accurate beam forming.

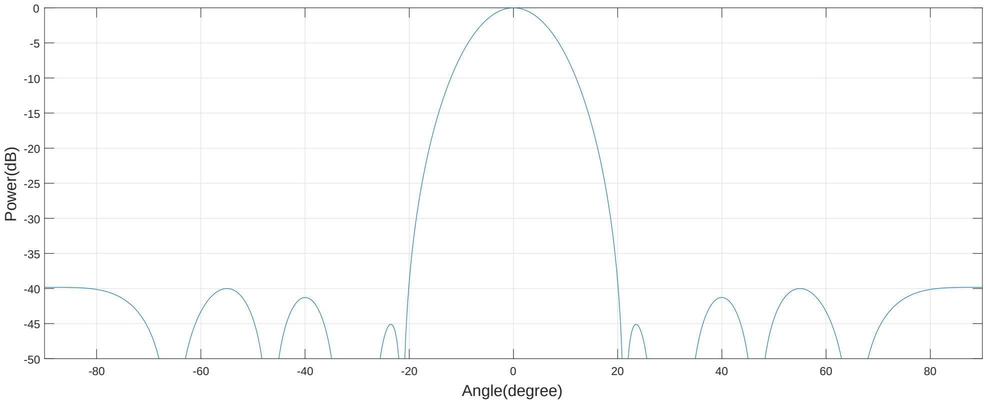

Fig. 3.3: A slice of the beam pattern for 11×11 rectangular array with Hamming weight in logarithmic scale. Sidelobes are extremely low that the disturbance can be suppressed to a low level in beam tracking.

The beam pattern obtained by Hamming weight is provided in Figs. 3.2 and 3.3, which show a relatively good suppression of sidelobes.

In order to more effectively change the beam direction with the smart phone's movement, beam steering is employed instead of beam switching adopted in [42]. Beam steering can be achieved by adjusting the phase shift variables, of which θ_0 and ϕ_0 are the desired steering angles calculated from the LoS vector.

$$\begin{aligned} B_0(\psi_x, \psi_y) &= e^{-j(\frac{N-1}{2}\psi_x + \frac{M-1}{2}\psi_y)} \\ \sum_{m=0}^{M-1}\sum_{n=0}^{N-1} & w_{nm}^{*} e^{j(n(\psi_x+\beta_x)+m(\psi_y+\beta_y))}] \end{aligned} \tag{3.18}$$

where

$$\beta_x = \frac{2\pi}{\lambda}\sin\theta_0\cos\phi_0 \tag{3.19}$$

$$\beta_y = \frac{2\pi}{\lambda}\sin\theta_0\sin\phi_0 \tag{3.20}$$

3.4 The Proposed Tracking Algorithm

The proposed overall tracking algorithm is illustrated in the flowchart in Fig. 3.4. The proposed technique incorporates the 5G cellular network and a smartphone to aid the beam tracking operation. When the UN enters the coverage of a 5G network, it will synchronise with the AN at the first place, and the uplink signal will be processed for beam training to initialise joint DoA/ ToA EKF localisation tracking, as presented in section 3.2. The localisation tracking algorithm will operate and keep running through the whole process of the communication to update the state vector of equation (3.1). The location information obtained from joint DoA/ToA will be applied for sensor fusion to establish and maintain the beam alignment. The sensor fusion algorithm is for tracking the rotation information, which is shown in section 2.3, and the beam steering algorithm is introduced in equation (3.18). If the received signal power drops below a predefined threshold, the network system will trigger neighbour ANs to scan for the UN's beam and one AN with maximum power link to the UN will be established. As for the UN's beam, the beam pattern is illustrated in section 3.3. After getting connected with another AN, the whole process will be performed again to maintain the quality of the communication link.

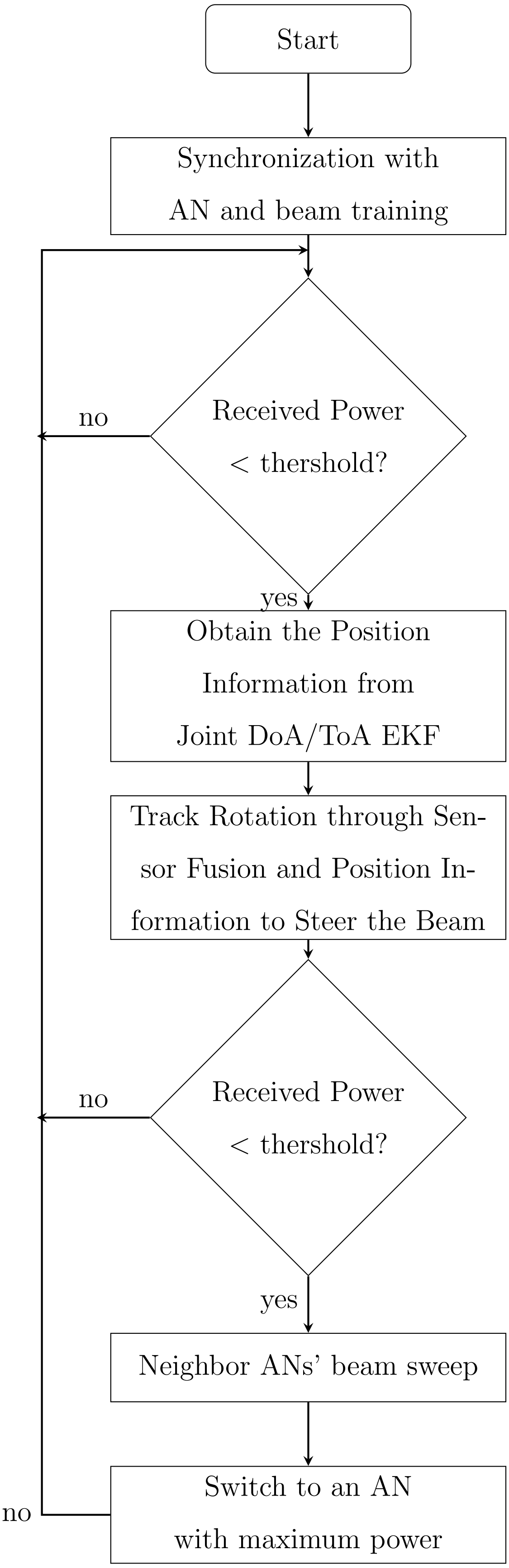

Fig. 3.4: Flowchart of proposed beam tracking process.

3.5 Simulation Results

In this section, the performance of the proposed algorithm is examined in three different scenarios. The first one is self-rotation with a fixed UN position and one AN, the second one is self-rotation with the straight-line movement of the UN in a short distance and one AN, and the third one is self-rotation with the straight-line movement of the UN along with a long distance and six ANs. For simplicity, the multipath effect and the transmission and handover time are not considered in this thesis.

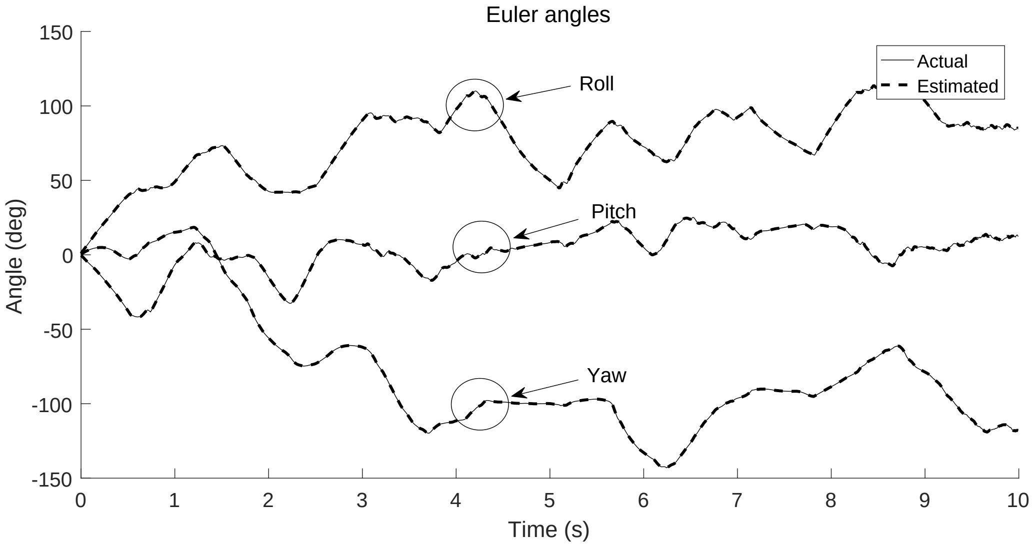

Fig. 3.5: Self-rotaion tracking result. The first 10 seconds operation of rotation is presented.

For all the scenarios, the setting of self-rotation tracking simulation is the same. The initial state is (0m, 0m, 0m), the UN is at the origin in the coordinate and m means metre, for all the sensors and the gyroscope error magnitude β is set to be 0.1 according to [44]. The delay of sensor measurements can be ignored as it is at the order of nanoseconds. The delay of beam steering is picoseconds and can be ignored too [52], and the operation time is 30s. The self-rotation tracking result for the first 10 seconds is shown in Fig. 3.5. The RMSEs of yaw-roll-pitch angle are 1.1530°, 0.5920° and 0.4937° for the self-rotation tracking results, respectively. Compared to [53], the result indicates that the self-rotation tracking algorithm has achieved a high level of accuracy.

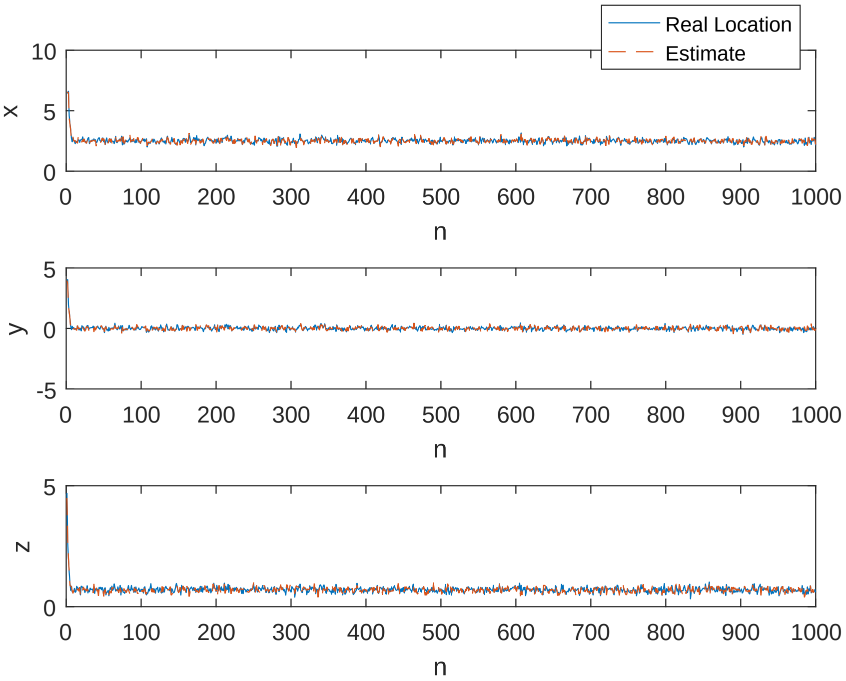

Fig. 3.6: Localisation tracking result for scenario 1. The UN stands at a fixed position with a predefined rotation and one AN. This figure shows the first 1000 iterations and n is the update index number.

In the first scenario, the UN stands at a fixed position with a predefined self-rotation rate and one AN. The location tracking EKF employed here is initialized with a coarse estimate obtained from GPS, DoA or some other commercial position systems, since the initial value only has a very limited impact on the following tracking process [48]. The update period

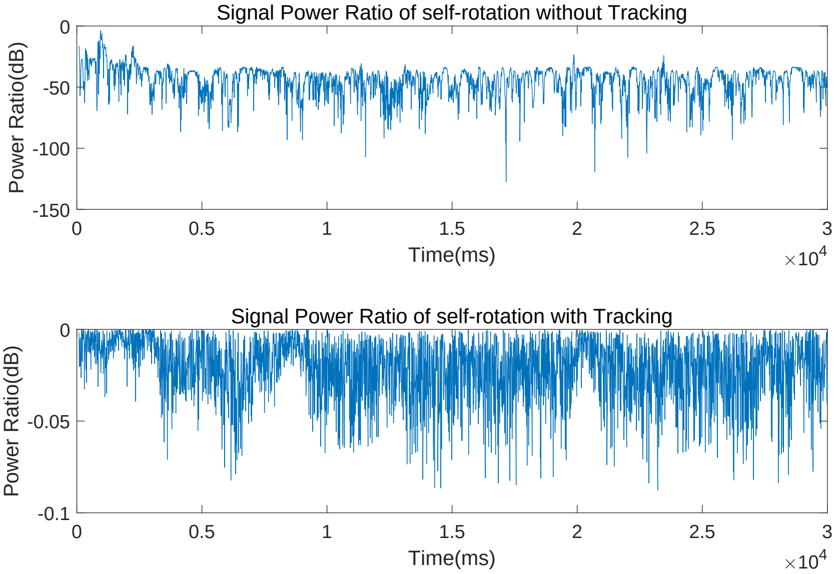

Fig. 3.7: Signal power with and without tracking for scenario 1. The operation time is 30 seconds. The scenario setting is as the same as in Fig. 3.6. Signal power ratio is calculated as the ratio between the received power and the transmitted power.

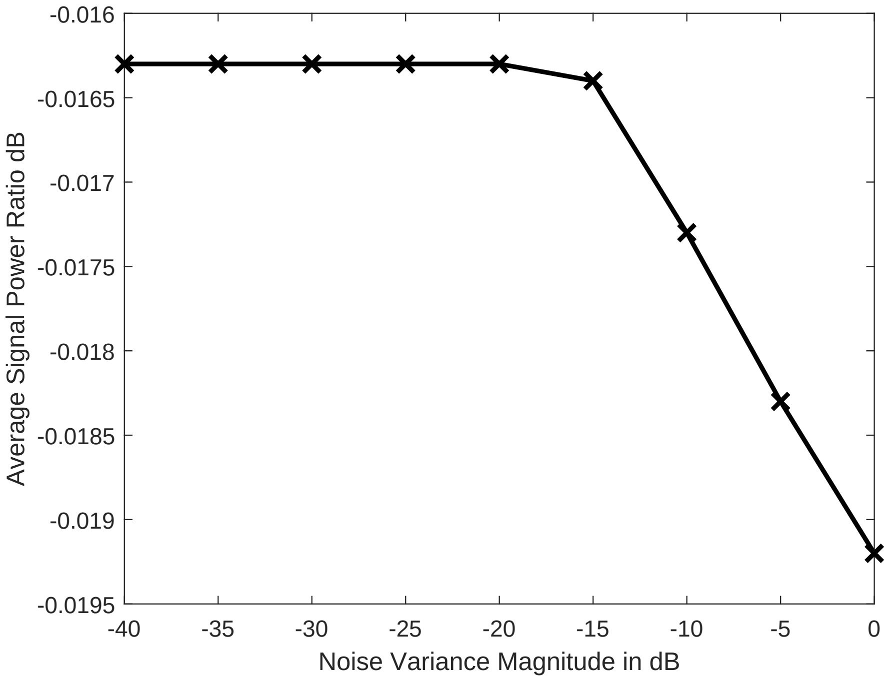

Fig. 3.8: Average signal power ratio with different SNRs for scenario 1. The scenario setting is as the same as in Fig. 3.6. Nine different SNRs with the correspondent signal power ratio are displayed in this figure.

is $T_t = 167.3\mu s$ [8]. The target starts at state $\boldsymbol{s} = [0 \quad 0 \quad 0 \quad 1 \quad 0 \quad 0]^T$. Within the update cycle, the noise variance magnitude of DoA and ToA is set to be 0.1. The update process follows the equations from (3.6) to (3.10). The tracking result for the first 1000 iterations is shown in Fig. 3.6, with n being the update index number. We can see that the location of UN is estimated at around ($2.5m$, $0m$, $0.7m$) and the calculated RMSE is $0.9603m$.

The location information of UN is used in the following beam tracking process and the beam tracking results are presented in Fig. 3.7 for the three rotation angles. We can see that for the case without tracking, the signal power has dropped to a very low level destroying the communication link entirely. In contrast, the sensor-aided tracking method provides continuous high signal power during the process. In Fig.3.8, average signal power with different SNRs is presented, the signal power ratio keeps all above -2dB from 0dB to 40dB.

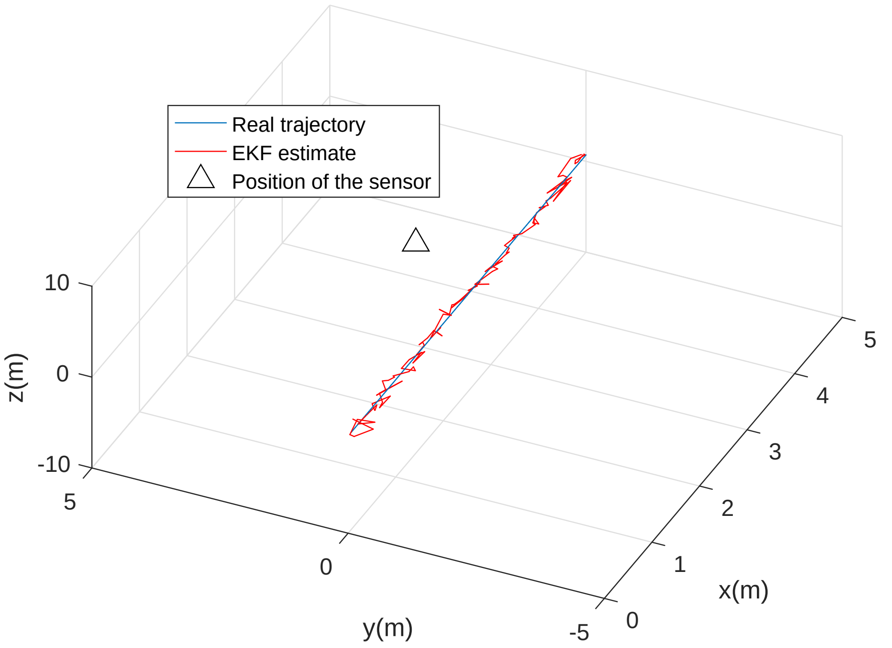

Fig. 3.9: Localisation tracking result in 2D for scenario 2. The UN moves along a 5 meters straight line at a constant speed for ten seconds.

In the second scenario, the UN moves along a 5-meter straight line at a constant speed for $10s$ and communicates with one AN. The AN is placed at the middle of the trajectory at position ($5m$, $1m$, $5m$). A 3-D location tracking result is shown in Fig. 3.9. It is clear that, the localization is quite accurate in 5-meter movement with a RMSE of $0.9612m$.

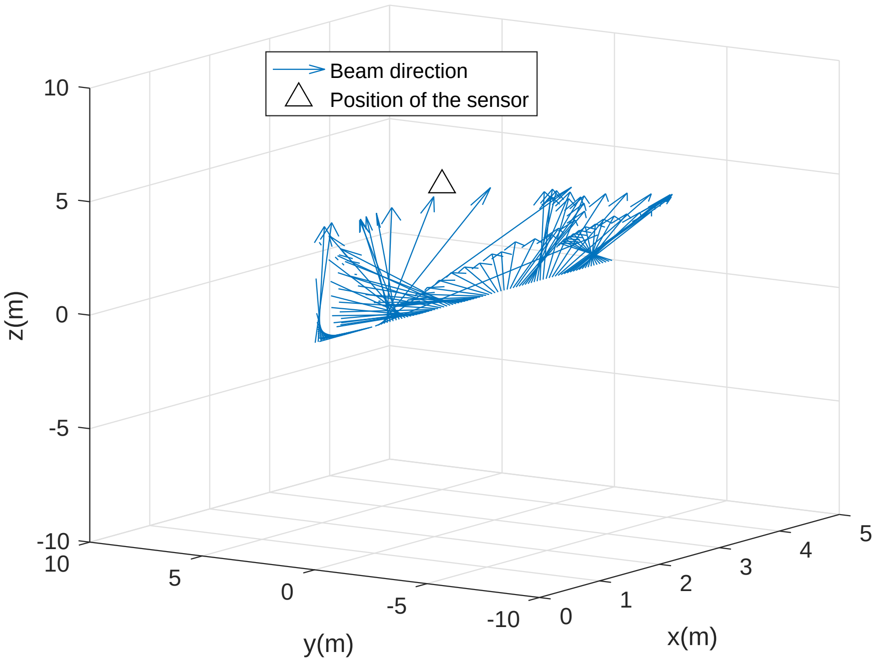

Fig. 3.10: UN beam directions without tracking for scenario 2. The scenario setting is as the same as in Fig. 3.9. The beam direction is shown as the arrow in the figure and the position of the sensor is marked as a triangle.

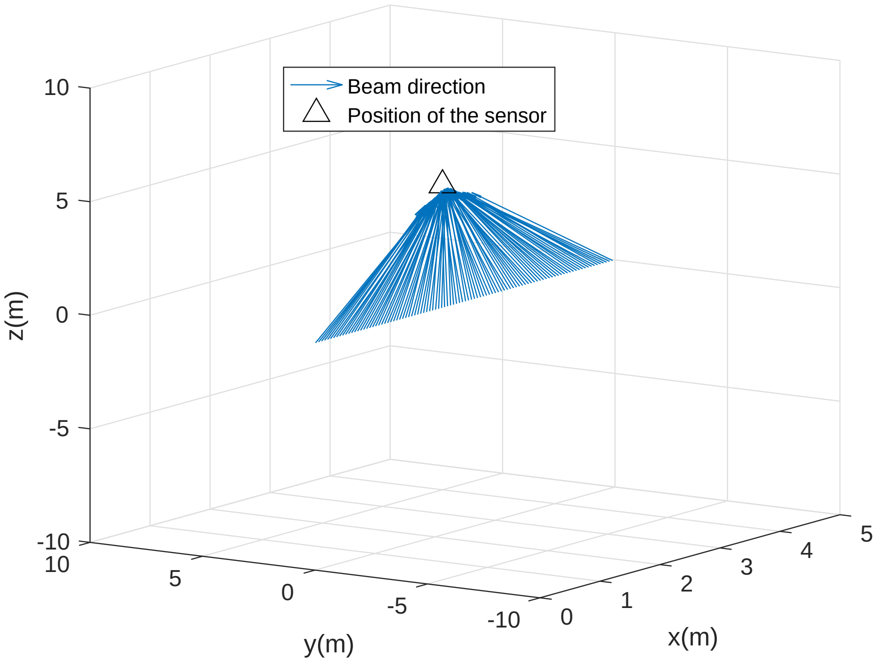

Fig. 3.11: UN beam directions with tracking for scenario 2. The scenario setting is as the same as in Fig. 3.9. The beam direction is shown as the arrow in the figure and the position of the sensor is marked as a triangle.

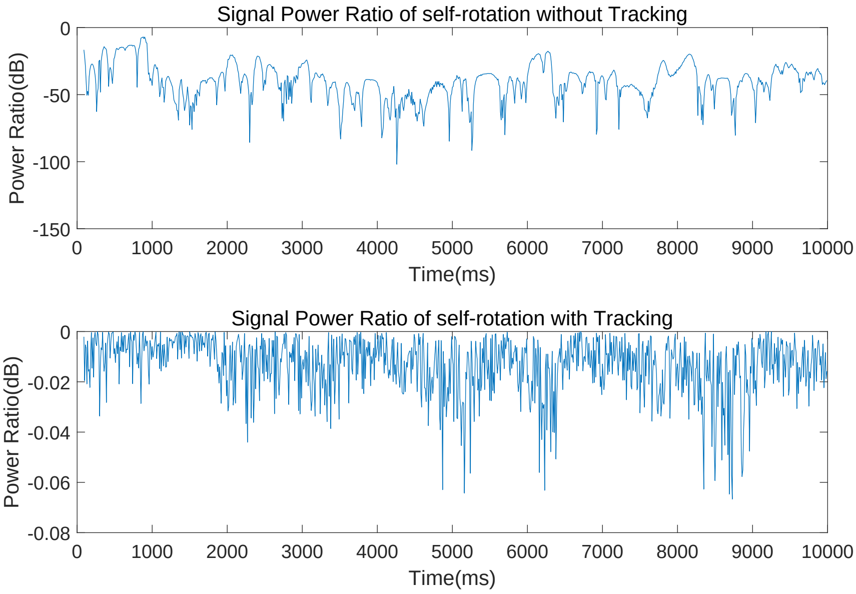

Fig. 3.12: Signal power with and without tracking for scenario 2. The scenario setting is as the same as in Fig. 3.9. Signal power ratio is calculated as the ratio between the received power and the transmitted power.

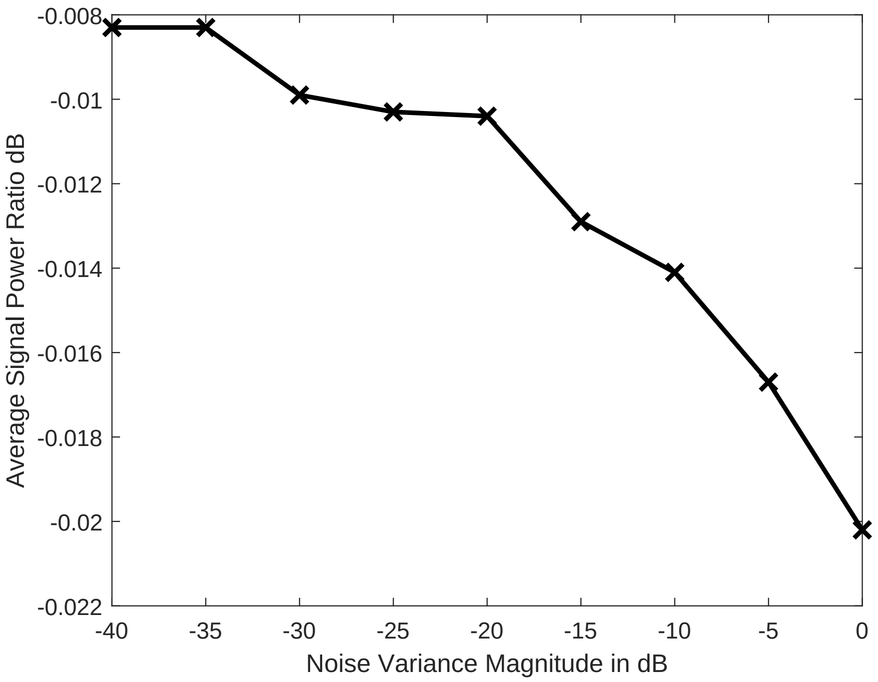

Fig. 3.13: Average signal power ratio with different SNRs for scenario 2. The scenario setting is as the same as in Fig. 3.9. Nine different SNRs with the correspondent signal power ratio are displayed in this figure.

It can be seen from Figs. 3.10 and 3.11 that without tracking the directions of the beam point to random directions and with tracking the beams have been focused towards the AN. Note that for convenience to visualize, only some sampled points are displayed in Figs. 3.10 and 3.11. The received signal power is shown in Fig. 3.12 and average signal power with different SNRs in Fig.3.13, and we can see that the received power stays at a high level to keep the connection in the process even with low SNR.

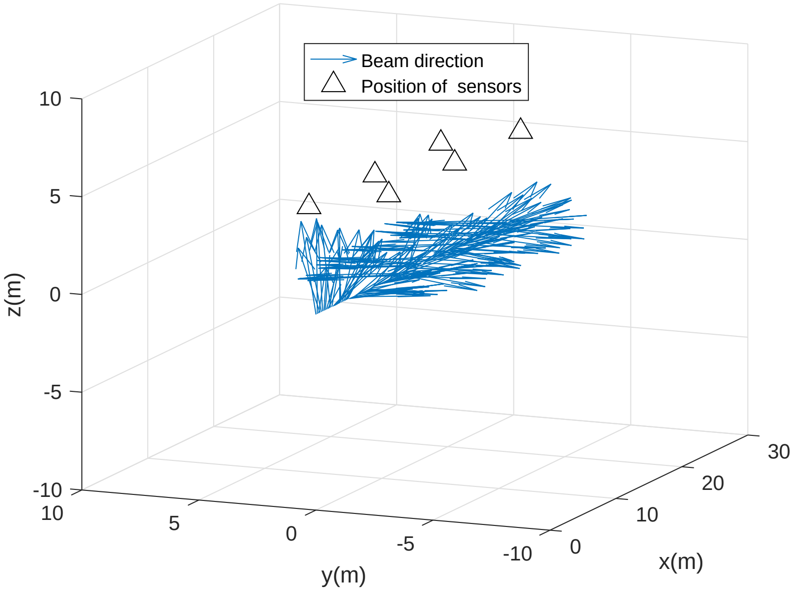

Fig. 3.15: UN beam directions without tracking for scenario 3. The scenario setting is as the same as in Fig. 3.14. The beam direction is shown as the arrow in the figure and the position of the sensor is marked as a triangle.

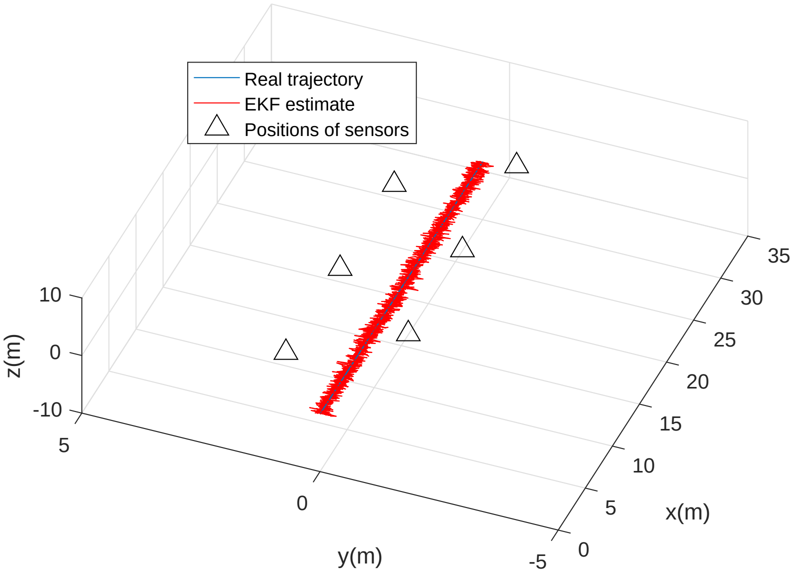

Fig. 3.14: Localisation tracking result in 2D for scenario 3. The UN moves along a 30 meters straight line at a constant speed for 30 seconds with 6 ANs.

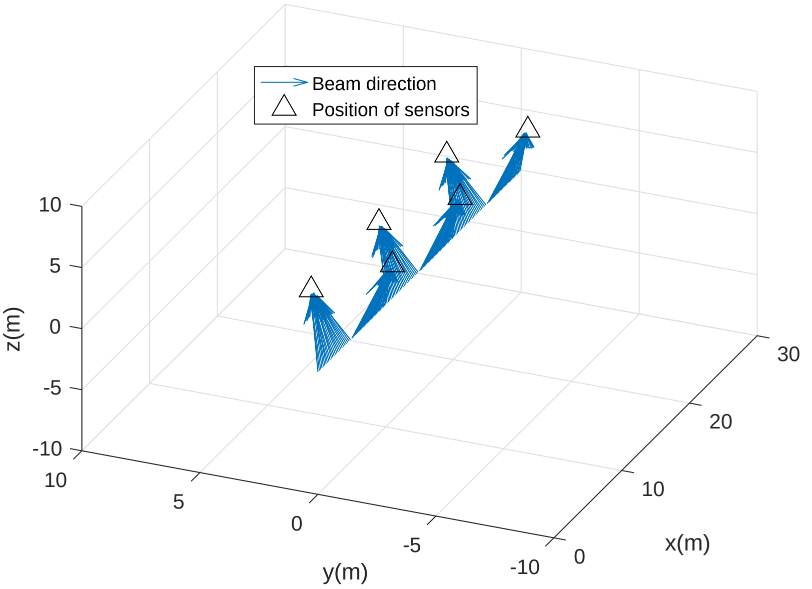

Fig. 3.16: UN beam directions with tracking for scenario 3. The scenario setting is as the same as in Fig. 3.14. The UN switches the connection with the AN every 5 meters. The beam direction is shown as the arrow in the figure and the position of the sensor is marked as a triangle.

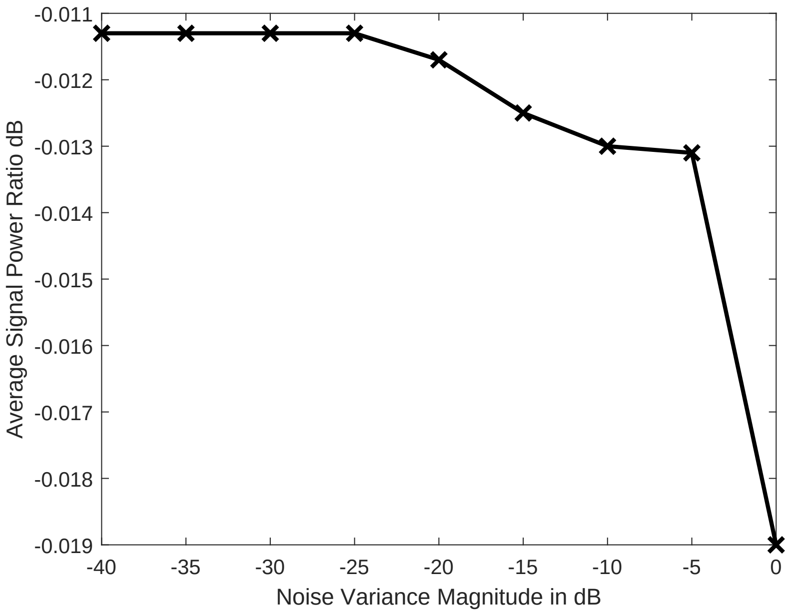

Fig. 3.18: Average signal power ratio with different SNRs for scenario 3. The scenario setting is as the same as in Fig. 3.14. The UN switches the connection with the AN every 5 meters. Nine different SNRs with the correspondent signal power ratio are displayed in this figure.

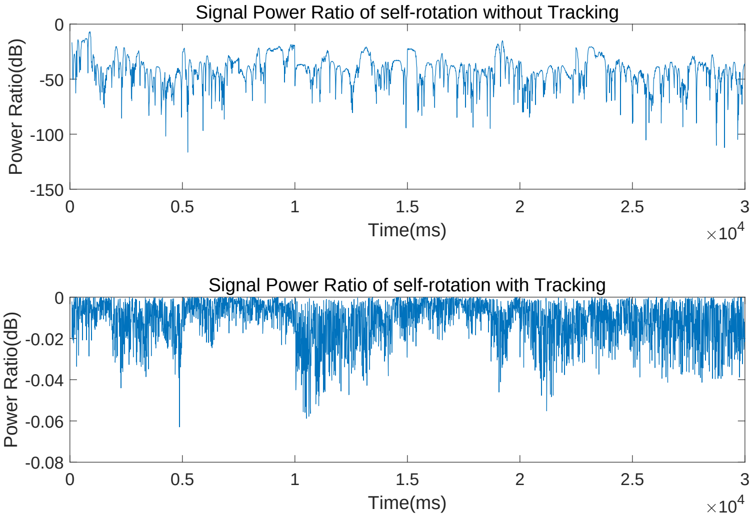

Fig. 3.17: Signal power with and without tracking for scenario 3. The scenario setting is as the same as in Fig. 3.14. The UN switches the connection with the AN every 5 meters. Signal power ratio is calculated as the ratio between the received power and the transmitted power.

In scenario three, the UN moves along a 30 meters straight line at a constant speed for 30 seconds with 6 ANs. During the process, the UN switches the connection with the AN every 5 meters. And the result and demonstration of the process is shown in Fig. 3.14 at an RMSE of $0.9625m$. It can be seen from the comparison between Figs. 3.15 and 3.16 that the beam of the tracking aided UN has always been pointing to the right AN, while the beam direction without tracking looks like a random process. The received signal power also stays at a high level in Fig. 3.17 and Fig.3.18 with different SNRs, all above -0.06dB.

Chapter 4

Conclusion

A new 3-D millimetre wave beam tracking method with network level implementation has been proposed. There are two parts in the proposed method: one is the self-rotation tracking using three embedded smart phone sensors based on a gradient descent algorithm; the other one is location tracking using a combination of DoA and ToA information through extended Kalman filtering. We showed that the proposed method can achieve high accuracy beam tracking tasks in three differnet scenarios: one is with a fixed UN location and one AN involved, while the other two are with a steady straight-line movement, but with different number of ANs involved. We find that the proposed method can tackle with millimetre wave transmission tasks. Finally, we suggest futher research in channel model to give a more realistic setting in the method.

Chapter 5

Future Plan

The proposed tracking method is preliminary that all the settings have been considered as being idealised. So for the future work, some more realistic models will be proposed and tested. Explicitly, potential improvements to the current algorithm are presented in following parts.

5.1 Channel Model

The 5G ultra-dense network in the future will enable one user to operate under several ANs [54], which renders a single-input-multiple-output channel(SIMO). Since ANs and UNs in 5G network are likely to be equipped with antenna array or re-configurable antennas [21] and the uplink reference signal are assumed to be orthogonal frequency-division multiplexing, and the channel model will be modelled as single-input-multiple-output multiple antenna-multiple-carrier channel [54]. Based on the literature, [55] has proposed a suitable channel model to simulate a realistic 5G multipath

Channel. The general form of this model is as follows,

$$\boldsymbol{g} \approx \mathbf{B}\boldsymbol{\gamma} + \boldsymbol{n} \tag{5.1}$$

where g is the multichannel vector, **B** and $\boldsymbol{\gamma}$ represents the polarimetric response and path weights respectively.

My future work is to try to modify this model to make it fit in my algorithm. The challenge of this work is about incorporating handset rotation information (represented in the form of quaternion) and linking it with the rotation tracking algorithm in this model. The computation complex is low, the time estimate for mathematical derivation and programming would be finished in one to two months.

5.2 Tracking Method

The assumption made in this report is that the ToA clock synchronisation is perfect, however, in the real situation, the clock synchronisation is very hard to be perfect. But, in 5G ultra-dense network, radio frames of radio networks are expected to be in the order of 0.1-0.5 ms [8]. These frames are essential in tracking methods used in this report to be the reference signal for ToA. Since the frame is very short, the expected errors are also small. However, these errors could not be ignored, so a clock compensation is needed for my model. In the literature, [19] has proposed a ToA clock compensation by assuming synchronised UNs by applying Unsent Kalman filtering (UKF). The model they are using is quite easy, but the configuration in UKF requires furrier transform, which makes the system complicated.

Understanding the clock compensation method and how to apply it in the algorithm would be my first step in the future work. Then, trying to modify the definition of the model to make it less complicated and fit it in my algorithm would be my next step.

5.3 NLoS identification Algorithm

Other than that, the scenario considered in the previous work assumes a UN connects only one AN every time. However, as being discussed before, multiple ANs may connect to one UN simultaneously. Loads of information including ToA, DoA, distance, channel information, signal strength and so on would be calculated and gathered all together. [56] has proposed a non-line-of-sight identification method based on one set of ToA, DoA and signal strength information. Loads of sets of this information would be ideal for detecting the obstacle in the AN-UN communication path.

My future work will be studying this method and modify it with the specific algorithm to combine all the information to render an accurate NLoS identification.

5.4 Extension to Other Scenarios

Other than the behavioural changes, [57] has pointed out that wind-induced vibrations of ANs are another problem of 5G communication. Indeed, the wind-induced changes need to be taken into considerations in my future work.

Bibliography

[1] Google, “Android developers,” 2017, [Accessed: 25 May, 2017]. [Online]. Available: http://developer.android.com/reference/

[2] K. N. Lee, *Compass and gyroscope: integrating science and politics for the environment.* Island Press, 1994.

[3] N. Ravi, N. Dandekar, P. Mysore, and M. L. Littman, “Activity recognition from accelerometer data,” in *Aaai*, vol. 5, no. 2005, 2005, pp. 1541–1546.

[4] R. Zekavat and R. M. Buehrer, *Handbook of position location.* Wiley, 2011.

[5] Huawei, “5G: A technology vision (white paper),” 2013, [Accessed: 25 Mar, 2016]. [Online]. Available: http://www.huawei.com/5gwhitepaper

[6] D. López-Pérez, M. Ding, H. Claussen, and A. H. Jafari, “Towards 1 Gbps/UE in cellular systems: Understanding ultra-dense small cell deployments,” *IEEE Communications Surveys & Tutorials*, vol. 17, no. 4, pp. 2078–2101, 2015.

[7] M. Ding, D. López-Pérez, G. Mao, P. Wang, and Z. Lin, “Will the area spectral efficiency monotonically grow as small cells go dense?” in *2015 IEEE Global Commun. Conf. (GLOBECOM)*, San Diego, CA, USA, Dec. 6-10 2015, pp. 1–7.

[8] P. Kela, M. Costa, J. Salmi, K. Leppanen, J. Turkka, T. Hiltunen, and M. Hronec, “A novel radio frame structure for 5G dense outdoor radio access networks,” in *IEEE 81st Veh. Tech. Conf. (VTC Spring)*, Glasgow, UK, May 11-14 2015, pp. 1–6.

[9] R. Baldemair, T. Irnich, K. Balachandran, E. Dahlman, G. Mildh, Y. Selén, S. Parkvall, M. Meyer, and A. Osseiran, “Ultra-dense networks in millimeter-wave frequencies,” *IEEE Commun. Mag.*, vol. 53, no. 1, pp. 202–208, 2015.

[10] C. X. Wang, F. Haider, X. Gao, X. H. You, Y. Yang, D. F. Yuan, H. Aggoune, H. Haas, S. Fletcher, and E. Hepsaydir, “Cellular architecture and key technologies for 5g wireless communication networks,” *IEEE Commun. Mag.*, vol. 52, no. 2, pp. 122–130, 2014.

[11] F. Boccardi, R. W. Heath, A. Lozano, T. L. Marzetta, and P. Popovski, “Five disruptive technology directions for 5g,” *IEEE Commun. Mag.*, vol. 52, no. 2, pp. 74–80, 2014.

[12] P. Stoica, E. G. Larsson, and A. B. Gershman, “The stochastic CRB for array processing: A textbook derivation,” *IEEE Signal Processing Letters*, vol. 8, no. 5, pp. 148–150, 2001.

[13] D. Dardari, P. Closas, and P. M. Djurić, “Indoor tracking: Theory, methods, and technologies,” *IEEE Trans. Veh. Technol*, vol. 64, no. 4, pp. 1263–1278, Apr. 2015.

[14] Z. Pan and Q. Zhu, “Modeling and analysis of coverage in 3-D cellular networks,” *IEEE Commun. Lett*, vol. 19, no. 5, pp. 831–834, 2015.

[15] K. Zheng, L. Zhao, J. Mei, B. Shao, W. Xiang, and L. Hanzo, “Survey of large-scale MIMO systems,” *IEEE Commun. Surveys & Tutorials*, vol. 17, no. 3, pp. 1738–1760, 2015.

[16] J. Medbo, I. Siomina, A. Kangas, and J. Furuskog, “Propagation channel impact on LTE positioning accuracy: A study based on real measurements of observed time difference of arrival,” in *IEEE 20th International Symposium on Personal, Indoor and Mobile Radio Communications*, vol. 4, 2009, pp. 2213–2217.

[17] H. Liu, Y. Gan, J. Yang, S. Sidhom, Y. Wang, Y. Chen, and F. Ye, “Push the limit of WIFI based localization for smartphones,” in *Proc. of the 18th Annu. Int. Conf. on Mobile Computing and Networking*, vol. 11, 2012, pp. 305–316.

[18] J. Werner, M. Costa, A. Hakkarainen, K. Leppanen, and M. Valkama, “Joint user node positioning and clock offset estimation in 5G ultra-dense networks,” in *IEEE Global Communications Conference (GLOBECOM)*, San Diego, CA, USA, Dec. 6-10 2015, pp. 1–7.

[19] M. Koivisto, M. Costa, A. Hakkarainen, K. Leppanen, and M. Valkama, “Joint 3D positioning and network synchronization in 5G

ultra-dense networks using UKF and EKF," in *Globecom Workshops (GC Wkshps), IEEE*, Washington, DC USA, December 4-8 2016, pp. 1–7.

[20] S. Jeong, J. Kang, K. Pahlavan, and V. Tarokh, "Fundamental limits of TOA/DOA and inertial measurement unit-based wireless capsule endoscopy hybrid localization," *International Journal of Wireless Information Networks*, vol. 24, no. 2, pp. 169–179, 2017.

[21] J. Werner, J. Wang, A. Hakkarainen, D. Cabric, and M. Valkama, "Performance and cramer–rao bounds for DoA/RSS estimation and transmitter localization using sectorized antennas," *IEEE Trans. Veh. Technol*, vol. 65, no. 5, pp. 3255–3270, 2016.

[22] X. Cheng, D. Zhu, S. Zhang, and P. He, "Tracking positioning algorithm for direction of arrival based on direction lock loop," *Future Internet*, vol. 7, no. 3, pp. 214–2242, Jun. 2015. [Online]. Available: http://www.mdpi.com/1999-5903/7/3/214/htm. [Accessed Jun. 18, 2016]

[23] H. J. Luinge and P. H. Veltink, "Inclination measurement of human movement using a 3-D accelerometer with autocalibration," *IEEE Trans. Neural Syst. Rehabil. Eng.*, vol. 12, no. 1, pp. 112–121, 2004.

[24] H. Zhou and H. Hu, "Human motion tracking for rehabilitation—A survey," *Biomedical Signal Processing and Control*, vol. 3, no. 1, pp. 1–18, 2008.

[25] D. Titterton and J. L. Weston, *Strapdown inertial navigation technology.* IET, 2004.

[26] S. Beauregard, "Omnidirectional pedestrian navigation for first responders," in *WPNC'07. 4th Workshop on Positioning, Navigation and Communication*, University of Hannover, Germany, March 22, pp. 33–36.

[27] B. Barshan and H. F. Durrant-Whyte, "Inertial navigation systems for mobile robots," *IEEE Trans. Robot. Autom.*, vol. 11, no. 3, pp. 328–342, 1995.

[28] L. Ojeda and J. Borenstein, "Flexnav: Fuzzy logic expert rule-based position estimation for mobile robots on rugged terrain," in *IEEE International Conference on Robotics and Automation*, vol. 1, 2002, pp. 317–322.

[29] M. Euston, P. Coote, R. Mahony, J. Kim, and T. Hamel, "A complementary filter for attitude estimation of a fixed-wing UAV," in *IEEE/RSJ Int. Conf. on Intelligent Robots and Systems*, Nice, France, September 22-26, pp. 340–345.

[30] S. K. Hong, "Fuzzy logic based closed-loop strapdown attitude system for unmanned aerial vehicle (UAV)," *Sensors and Actuators A: Physical*, vol. 107, no. 2, pp. 109–118, 2003.

[31] A. Kallapur, I. Petersen, and S. Anavatti, "A robust gyroless attitude estimation scheme for a small fixed-wing unmanned aerial vehicle," in *Asian Control Conference, 2009. ASCC*, August 27-29, pp. 666–671.

[32] J. E. Bortz, “A new mathematical formulation for strapdown inertial navigation,” *IEEE Trans. Aerosp. Electron. Syst.*, no. 1, pp. 61–66, 1971.

[33] M. Ignagni, “Optimal strapdown attitude integration algorithms,” *Journal of Guidance, Control, and Dynamics*, vol. 13, no. 2, pp. 363–369, 1990.

[34] N. Yazdi, F. Ayazi, and K. Najafi, “Micromachined inertial sensors,” *Proc. of the IEEE*, vol. 86, no. 8, pp. 1640–1659, 1998.

[35] H. Luinge, P. H. Veltink, and M. Baten, “Estimation of orientation with gyroscopes and accelerometers.” in *Technology and Health Care*, vol. 7, 1999, pp. 455– 459.

[36] J. Marins, X. Yun, E. Bachmann, R. McGhee, and M. Zyda, “An extended kalman filter for quaternion-based orientation estimation using marg sensors,” in *2001 IEEE/RSJ Inter. Conf. on Intelligent Robots and Systems*, vol. 4, 2001, pp. 2003–2011.

[37] A. M. Sabatini, “Quaternion-based extended kalman filter for determining orientation by inertial and magnetic sensing,” *IEEE Trans. Biomed. Eng.*, vol. 53, no. 7, pp. 1346–1356, 2006.

[38] H. J. Luinge and P. H. Veltink, “Measuring orientation of human body segments using miniature gyroscopes and accelerometers,” *Medical and Biological Engineering and computing*, vol. 43, no. 2, pp. 273–282, 2005.

[39] D. Jurman, M. Jankovec, R. Kamnik, and M. Topič, “Calibration and data fusion solution for the miniature attitude and heading reference system,” *Sensors and Actuators A: Physical*, vol. 138, no. 2, pp. 411–420, 2007.

[40] M. Haid and J. Breitenbach, “Low cost inertial orientation tracking with kalman filter,” *Applied Mathematics and Computation*, vol. 153, no. 2, pp. 567–575, 2004.

[41] M. Ruyg and S. Teunisse, C.and Verhage, “Virtual reality for the web: Oculus rift,” 2014.

[42] D. Shim, C. Yang, J. Kim, J. Han, and Y. Cho, “Application of motion sensors for beam-tracking of mobile stations in mmWave communication systems,” *Sensors*, vol. 14, no. 10, pp. 19 622–19 638, 2014. [Online]. Available: http://www.mdpi.com/1424-8220/14/10/19622/html. [Accessed Jun. 25, 2016]

[43] Z. Qi and W. Liu, “Three-dimensional millimetre wave beam tracking based on handset mems sensors with extended kalman filtering,” in *Radio Propagation and Technologies for 5G.* Durham, UK: IET, Oct.3, 2016, pp. 1–6.

[44] S. Madgwick, A. Harrison, and R. Vaidyanathan, “Estimation of IMU and MARG orientation using a gradient descent algorithm,” in *2011 IEEE Int. Conf. on Rehabilitation Robotics (ICORR)*, 2011, pp. 1–7.

[45] Z. Qi and W. Liu, “Three-dimensional millimetre wave beam tracking based on smart phone sensor measurements and DOA/TOA estima-

tion for 5G networks," *IET Microwaves, Antennas & Propagation*, vol. 12, no. 3, pp. 271–279, 2017.

[46] M. D. Jiang, Y. Li, and W. Liu, "Properties of a general quaternion-valued gradient operator and its application to signal processing," *Frontiers of Information Technology & Electronic Engineering*, vol. 17, pp. 83–95, February 2016.

[47] J. Diebel, "Representing attitude: Euler angles, unit quaternions, and rotation vectors," *Matrix*, vol. 58, no. 15-16, pp. 1–35, 2006.

[48] D. Simon, *Optimal State Estimation: Kalman, H Infinity, and Nonlinear Approaches*, 1st ed. Hoboken, N.J: Wiley-Interscience, Jun 2006.

[49] O. J. Woodman, "An introduction to inertial navigation," University of Cambridge, Computer Laboratory, Tech. Rep. UCAM-CL-TR-696, Aug. 2007. [Online]. Available: http://www.cl.cam.ac.uk/techreports/UCAM-CL-TR-696.pdf

[50] R. G. Valenti, I. Dryanovski, and J. Xiao, "Keeping a good attitude: A quaternion-based orientation filter for IMUs and MARGs," *Sensors*, vol. 15, no. 8, pp. 19 302–19 330, 2015.

[51] W. Liu and S. Weiss, *Wideband Beamforming: Concepts and Techniques*. Chichester, UK: John Wiley & Sons, 2010.

[52] M. Longbrake, “True time-delay beamsteering for radar,” in *Aerospace and Electronics Conference (NAECON), IEEE National.* Dayton, OH, USA: IEEE, 2012, pp. 246–249.

[53] J. Hartikainen, A. Solin, and S. S. Särkkä, “Optimal filtering with Kalman filters and smoothers—a manual for matlab toolbox ekf/ukf,” 2008.

[54] A. Osseiran, F. Boccardi, V. Braun, and et al., “Scenarios for 5G mobile and wireless communications: the vision of the METIS project,” *IEEE Commun. Mag.*, vol. 52, no. 5, pp. 26–35, 2014.

[55] M. Koivisto, M. Costa, J. Werner, K. Heiska, J. Talvitie, K. Leppänen, V. Koivunen, and M. Valkama, “Joint device positioning and clock synchronization in 5G ultra-dense networks,” *IEEE Trans. Wireless Commun.*, vol. 16, no. 5, pp. 2866–2881, 2017.

[56] K. Yu and Y. J. Guo, “Statistical NLOS identification based on AOA, TOA, and signal strength,” *IEEE Trans. Veh. Technol.*, vol. 58, no. 1, pp. 274–286, 2009.

[57] S. Y. Hur, T. Kim, D. J. Love, J. V. Krogmeier, T. A. Thomas, and A. Ghosh, “Millimeter wave beamforming for wireless backhaul and access in small cell networks,” *IEEE Trans. Wireless Commun.*, vol. 61, no. 10, pp. 4391–4403, 2013.